
Politecnico di Torino


## Politecnico di Torino

Master's Degree in Mechatronic Engineering

A.a. 2025/2026

Graduation Session March 2026


# Model-Based Comparative Analysis of Lunar Rover Locomotion Systems

### A Multibody Dynamics Approach


Supervisor:

Prof. Fabrizio Stesina

Ing. Daniele Catelani

Candidate:

Lorenzo Caraccio, 317546

**Abstract**

The current expansion of space exploration, driven by international programs such as Artemis and Moonlight, is shifting the focus toward establishing permanent human settlements on the lunar surface. In this context, the development of robotic locomotion systems capable of operating in extreme and heterogeneous environments, such as the lunar South Pole, represents one of the most complex engineering challenges. This thesis presents a model-based comparative analysis to evaluate different locomotion architectures for a medium-sized lunar rover.

The research focuses on four candidate configurations: the flight-proven Rocker-Bogie (RB), used as a reference; the Double-Bogie (2BG), a simplified passive configuration; the Four-Wheel Active (4WA), an independent active suspension system; and an articulated Hybrid (HBD) model capable of multimodal locomotion. The methodology employs multibody dynamics (MBD) simulations within the MSC Adams environment.

Performance was quantified through three test scenarios termed Design Reference Missions (DRMs): steep slope climbing (30°), obstacle negotiation (30 cm), and steering capabilities. The results were integrated into a Systems Engineering framework using the Analytic Hierarchy Process (AHP), utilizing pairwise comparison matrices to perform a rigorous trade-off between dynamic metrics (energy consumption, payload stability, and critical speed) and static parameters (total mass and system complexity).

The comparative analysis identifies the Rocker-Bogie architecture as the optimal solution for the target mission objectives, demonstrating the best balance between operational efficiency and design feasibility. This study provides a neutral methodological basis for future design decisions, highlighting how the active adaptability of 4WA and HBD systems offers significant advantages in platform stability at the cost of increased control complexity and power consumption.

# Table of Contents

# List of Figures

# List of Tables

# Chapter 1

# Introduction

Lunar surface exploration has entered a new phase in the history of human technological progress. Driven by international programs such as NASA's Artemis [1] and ESA's Moonlight [2], access to the Moon is being significantly enhanced, transitioning from sporadic sorties to a sustained human and robotic presence. In this context, the design and deployment of planetary rovers represent one of the most complex challenges in space engineering, requiring a seamless integration of mechanical robustness, autonomous control, and environmental adaptability.

## 1.1 Lunar exploration context

As lunar missions evolve toward the establishment of permanent outposts, the requirement for high-performance locomotion systems has become a central focus for space agencies worldwide. Among the various landing sites under consideration, the exploration of the lunar South Pole is expected to be crucial for the success of future human settlements.

This region is of central interest due to the coexistence of areas of near-constant solar illumination, known as Peaks of Eternal Light (PELs)[3], and Permanently Shadowed Regions (PSRs)[4]. These PSRs, often referred to as "cold traps," are of strategic importance as they contain confirmed deposits of water ice.

The geographic significance of this area is further emphasised by its potential to serve as a stepping stone for deep-space missions. The ability to extract and

process local resources, a strategy known as In-Situ Resource Utilization (ISRU), will be fundamental to reducing Earth-dependency and enabling the long-term sustainability of space exploration. Consequently, the development of mobility platforms capable of operating in these extreme and heterogeneous environments is a prerequisite for the next generation of lunar surface operations.

## 1.2 Objectives

The primary objective of this research is to perform a comprehensive comparative analysis and trade-off of different locomotion architectures for a mid-sized lunar rover. As mission requirements become increasingly demanding, selecting the optimal mechanical configuration is no longer a task that can rely solely on heritage designs. Instead, it requires a rigorous, data-driven approach capable of evaluating performance under realistic dynamic conditions.

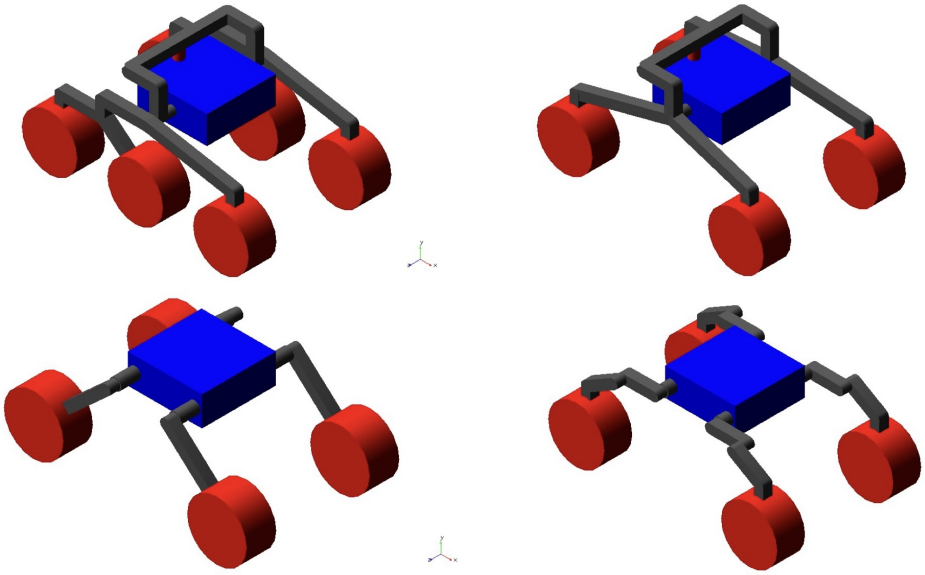

**Figure 1.1:** *Rover architectures*

To achieve this, the thesis focuses on four candidate architectures, each representing a different approach to lunar mobility:

- **Rocker-Bogie [RB]** used as reference, characterized by a passive suspension

system and steering mechanism

- **Double-Bogie** [**2BG**], a simplified passive configuration characterized by a skid-steering mechanism.
- **4-Wheel Active** [**4WA**], a simplified active configuration characterized by a skid-steering mechanism.
- **Hybrid/Articulated** [**HBD**], a disruptive articulated active configuration characterized by a steering mechanism

The scope of this work covers the full evaluation process, starting from high-fidelity modeling and leading to the final architectural choice. This study uses Multibody Dynamics (MBD) simulations in MSC Adams [5] to calculate specific performance metrics, known as Figures of Merit (FOMs). These metrics are collected across three key test scenarios, or Design Reference Missions (DRMs): **climbing steep slopes**, **crossing obstacles**, and **evaluating steering efficiency**. By integrating these simulation results into a Systems Engineering framework, this thesis aims to provide a technically justified selection that balances operational performance, payload safety, and system complexity. The ultimate goal is to define which architecture offers the most robust solution for the upcoming challenges of the Lunar South Pole exploration.

## 1.3 Thesis structure

Following the logical progression of work, from initial requirement analysis to the final trade-off selection, the thesis work is structured as follows:

- *Chapter 1* contains the context of lunar exploration and defines the objective of the thesis work.
- *Chapter 2* contains the state of the art of robotic platforms for space exploration and identification of key solutions in locomotion design
- *Chapter 3* defines the theoretical basis of multibody dynamics, contact mechanics, control theory, and system engineering principles used for the decision-making process

- *Chapter 4* defines mission requirements that drive the design of the robotic platform
- *Chapter 5* describes the selection of the Figures of Merit (FOMs) and test scenarios (DRMs) used to compare the performance
- *Chapter 6* contains the implementation of the chosen geometry and system requirements in **MSC Adams** software to develop the four model characteristics of each architecture
- *Chapter 7* presents the results obtained from simulation and performs comparative analysis for each DRM
- *Chapter 8* presents the results of trade-off analysis used to identify the optimal architecture and future development

# Chapter 2

# State of the art

Historically, the development of planetary rovers has been dictated by the "single-mission" paradigm. Each vehicle was conceived as a monolithic system, specifically engineered to survive the unique environmental conditions and topographical challenges of a predetermined landing site. This design philosophy prioritized specialized, integrated solutions over versatility, ensuring that the rover possessed a set of skills perfectly calibrated for a specific geographical area.

## 2.1 State of the art of lunar rovers

For this reason, the chronological evolution of these unmanned platforms demonstrates a progressive increase in system complexity and operational autonomy. Specifically for the lunar environment, the Soviet Lunokhod series (1970s) [6], developed as part of the Lunokhod programme (1969-1977), established the first standards for robotic lunar mobility. Utilizing an 8-wheel rigid-chassis design, these rovers served as technology demonstrators aimed at conducting the first in-situ studies of lunar soil composition.

In recent years, lunar exploration has seen a significant resurgence. Notable examples include the Chinese rovers Yutu (2013), part of the Chang'e 3 mission [7], and Yutu-2 (2019), part of the Chang'e 4 mission [8]. While the former focused on regolith composition, the latter achieved the historic objective of exploring the lunar far side. Similarly, the Indian rover Pragyan (2019), within the Chandrayaan

programme [9], provided critical data by discovering traces of water molecules on the surface. These three vehicles all rely on the passive Rocker-Bogie suspension, which is a standard choice for its ability to cross uneven terrains without the need for active actuators.

Finally, NASA's VIPER rover (2024)[10], a key precursor to the Artemis program, introduces a more advanced four-wheel active suspension system. The objectives of the VIPER mission are twofold: to study regolith properties in Permanently Shadowed Regions (PSRs) and to map the distribution of water ice. Unlike its predecessors, VIPER's active architecture is designed to overcome the risk of soil failure through specialized locomotion strategies, marking a shift toward more agile and performant mobility systems.

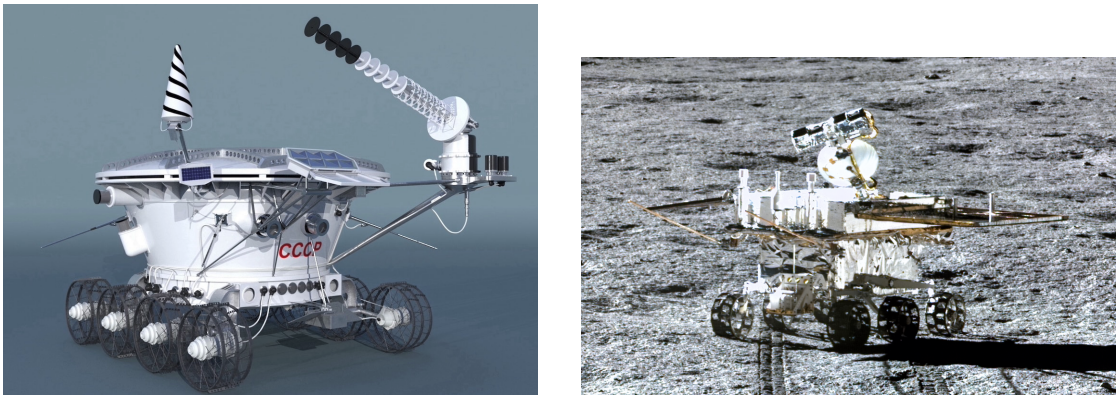


**Figure 2.1:** *Lunokhod 1 (left) and Yutu-2 (right)*

## 2.2 State of the art of Martian rovers

The exploration of Mars has established the Rocker-Bogie suspension as the definitive operational standard for planetary mobility. This passive architecture has been successfully utilized across a wide range of mission scales, starting from the Sojourner (1997)[11] and continuing through the Spirit and Opportunity (2003)[12] missions. The system was further scaled for the Curiosity (2011)[13] and Perseverance (2020)[14] rovers, proving its reliability in traversing the rugged Martian surface over long durations.

**Figure 2.2:** *Sojourner (left) and Perseverance (right)*

Despite this historical success, the current shift in space exploration toward long-term sustainability is introducing new challenges to traditional design approaches. As mission scenarios evolve to meet the needs of space agencies and commercial partners, the requirement for operational versatility is increasingly prioritized. Consequently, modern planetary rovers are transitioning from tailored projects and mission-specific designs toward more modular and reconfigurable platforms.

In this new framework, a locomotion system is expected to possess a broader set of capabilities, including the ability to adapt its kinematics to diverse terrains and perform complex maneuvers. While advanced architectures require a higher energy cost compared to fully passive solutions, the trade-off is often justified by the significant gain in flexibility and agility. The engineering focus is thus shifting from minimizing energy consumption as the unique metric to maximizing adaptability through active control. This represents a fundamental evolution in how planetary mobility is developed, bridging the gap between traditional space exploration and modern terrestrial robotic innovations, explained in the following section.

## 2.3 Key technological drivers in surface robotics

The modern evolution of robotic exploration is deeply linked with the progress of terrestrial autonomous systems. The primary technological drivers defining the current operational boundaries of planetary rovers are:

- **Autonomous navigation**: there is a significant transition from manual control toward high-level autonomy. This shift is driven by advancements in Simultaneous Localization and Mapping (SLAM), vision-based navigation, and machine learning algorithms for real-time hazard detection. These technologies enable rovers to traverse unstructured terrains, substantially increasing mission efficiency.

- **Power systems and thermal management**: Surviving the extreme thermal cycles of the lunar environment is made possible by modern advancements in thermal insulation and battery utilization derived from the electric vehicle industry.

- **Mobility system**: While the Rocker-Bogie configuration remains the flight-proven reference for passive stability, new concepts are emerging from terrestrial robotics, such as legged, hybrid, or highly articulated systems, designed to access extreme topographies inaccessible to traditional platforms.

A significant synergy is emerging between terrestrial and space robotics. The technology transfer of industrial know-how into space applications is evident in domains such as autonomous logistics, remote sensing, and environmental monitoring, as well as in fields like mining, defense, and Search and Rescue (SAR). Furthermore, advancements in artificial intelligence, telecommunications, and additive manufacturing are reducing costs and accelerating the development of next-generation space systems.
In conclusion, to provide a comprehensive overview of the systems discussed, the following table summarizes the technical specifications of the key planetary rovers mentioned in this chapter. This comparison highlights the evolution from historical passive standards to the modern active architectures targeted in this work, focusing on mass, locomotion type, and operational environment.

Having established the historical and technological framework of planetary mobility, the focus shifts toward the analytical approach. The following chapter describes the methodologies and software tools employed for the comparative analysis to perform a rigorous data-driven evaluation of the selected architectures.

**Table 2.1:** *Comparative analysis of planetary rovers state of the art.*

| **Name** | **Mission (Year)** | **Mass [kg]** | **Wheel** | **Mobility** | **Steer** | **Speed [m/s]** | **Env.** |
|---|---|---|---|---|---|---|---|
| Lunokhod 1 | Lunokhod (1970) | 840 | 8 | Passive | Skid | 0.2/0.55 | Lunar |
| Sojourner | Mars Pathf. (1997) | 11.5 | 6 | Rocker-Bogie | Explicit | 0.01 | Martian |
| Spirit and Opportunity | MER (2004) | 185 | 6 | Rocker-Bogie | Explicit | 0.05 | Martian |
| Curiosity | MSL (2011) | 899 | 6 | Rocker-Bogie | Explicit | 0.008 | Martian |
| Yutu | Chang'e 3 (2013) | 140 | 6 | Rocker-Bogie | Skid | 0.055 | Lunar |
| Yutu-2 | Chang'e 4 (2019) | 140 | 6 | Rocker-Bogie | Explicit | 0.055 | Lunar |
| Perseverance | Mars 2020 (2020) | 1025 | 6 | Rocker-Bogie | Explicit | 0.033 | Martian |
| Pragyan | Chandrayaan-3 (2023) | 26 | 6 | Rocker-Bogie | Skid | 0.01 | Lunar |
| VIPER | Artemis (2027) | 430 | 4 | Active | Explicit | 0.2 | Lunar |

# Chapter 3

# Methods and tools

## 3.1 Multibody Dynamics

Every complex machine is a multibody system; each of these systems is characterized by rigid or flexible bodies connected to each other by joints that could be fixed, rotational, spherical, and so on, which permits the description of the bodies' motion through roto-translation. The objective of a multibody dynamic analysis is the study of the body's equation of motion characterizing the movement and the force acting on the system and between the components of the system. A multibody system is described by the Lagrange equation [15], and in particular, the software MSC Adams describes the systems as follows :

The position of a rigid body is defined by the three Cartesian coordinates (x,y,z) and the three Euler angles ($\psi$, $\phi$,$\theta$).

$$\mathbf{p} = \begin{bmatrix} x \\ y \\ z \end{bmatrix}$$

$$\epsilon = \begin{bmatrix} \psi \\ \phi \\ \theta \end{bmatrix}$$

The set of generalized coordinates associated with the i-th body is expressed as follows :

$$\mathbf{q_i} = \begin{bmatrix} p_i \\ \epsilon_i \end{bmatrix}$$

Joint constraints are expressed by the relation:

$$\Phi(q) = 0 \tag{3.1}$$

meanwhile, actuators, representing a time-varying constraint, are expressed as:

$$\Phi(q, t) = 0 \tag{3.2}$$

Performing a dynamic analysis means solving the Lagrange equation:

$$\frac{d}{dt}\left(\frac{\partial L}{\partial \dot{q}_i}\right) - \frac{\partial L}{\partial q_i} + \sum_{k=1}^{m}\left(\frac{\partial \Phi_k}{\partial q_i}\right)\lambda_k = Q \tag{3.3}$$

Where **L** is the Lagrange function defined as:

$$L = K - P \tag{3.4}$$

In which **K** represents the total kinetic energy and $P$ the potential energy.

MSC Adams solver implements the following equation of motion for each body of the system :

$$[M]\ddot{\mathbf{q}} + \frac{d[M]}{dt}\dot{\mathbf{q}} - \frac{1}{2}\mathbf{q}^T\frac{\partial [M]}{\partial q}\dot{\mathbf{q}} + \frac{\partial P}{\partial q} + \Phi_d^T\lambda = Q \tag{3.5}$$

Where :

- $n$ is the number of bodies
- $m$ is the number of constraints
- $[M]$ is the $n \times m$ mass matrix
- $\frac{1}{2}q^T\frac{\partial [M]}{\partial q}\dot{q}$ is the total kinetic energy
- $\Phi_d$ is the $n \times m$ Jacobian matrix of the constraints

- $\lambda$ is the Lagrange multiplicator
- $Q$ is the n-th generalized force

MSC Adams uses different integrators to solve the system of differential equations that characterizes the multibody model, as explained in Adams Solver User's Guide [16]. The software provides a variety of numerical methods to manage the trade-off between calculation speed and numerical stability. In a multibody dynamic analysis, the choice of the integrator is fundamental to effectively solving the equations of motion and the constraints defined by the system's topology. The selection of the appropriate integrator ensures that the solver can maintain the required precision throughout the simulation time without leading to numerical divergence. In Table 3.1 a summary of different integrators is presented:

**Table 3.1:** *Overview of MSC Adams numerical integrators.*

| Integrator | Benefit | Model content |
|---|---|---|
| **GSTIFF I3** | • High calculation speed<br>• High accuracy of system displacements<br>• Robust in handling a variety of analysis problems | Recommended for most numerically stiff models (many mechanical systems with a large range of frequency content) and models with velocity inputs. |
| **GSTIFF SI2** | • Gives very accurate results, especially for velocities and accelerations<br>• Usually allows an ERROR that is approximately 10 to 100 times larger than regular GSTIFF to produce the same quality of results<br>• Is very robust and stable at small step sizes<br>• Corrector failures that small step sizes cause occur less frequently than with GSTIFF I3<br>• Singular matrices due to small step sizes occur less frequently than with GSTIFF I3<br>• Corrector failures are typically indicative of a modeling problem and not of a numerical deficiency in the MSC Adams Solver software<br>• Tracks high-frequency oscillations very accurately | Recommended for models where velocity or high-frequency accuracy might be important. Common examples include models with contact or friction |
| **HHT** | • Expected to result in a smaller number of Jacobian evaluations<br>• Unlike GSTIFF, it behaves like a low-pass filter; it cuts high-frequency spurious oscillations while accurately preserving low-frequency oscillations<br>• Can control the cutoff frequency by adjusting alpha; the smaller value (that is, closer to -0.3, the lower the cutoff threshold)<br>• Stable at small value of the integration step size | Recommended for fast solution of models with flexible bodies or those having high frequency content and/or durability loading. |

It is important to note that the integrators listed above are only a subset of those provided by the software. Other options, like WSTIFF and HASTIFF, can be used depending on the simulation's needs. Moreover, the choice of the solver engine determines which integrators are available. While the C++ solver is the current standard, some formulations, such as Constant BDF, RKF45, and ABAM, require the Fortran solver, whereas others, like HHT and Newmark, are specific to the C++ version.

## 3.2 Contact mechanics - Hertz theory

The mechanics of contact between bodies is explained by Hertz's theory [17], which predicts contact forces and geometrical deformation based on a set of assumptions:

- Adhesion between bodies is neglected, no adhesion forces occur during the separation of contact bodies
- Contact surface is smaller with respect to body dimensions
- Perfectly elastic materials

Considering two bodies in contact through the action of an applied force, the contact area depends on the geometry of the contact bodies, the load, and material properties. For example, two spheres or two cylinders crossed at 90° shows a circular contact area, for two parallel cylinders, the contact area is a narrow rectangle, meanwhile, in the case of two non parallel cylinders, the contact area is elliptical.

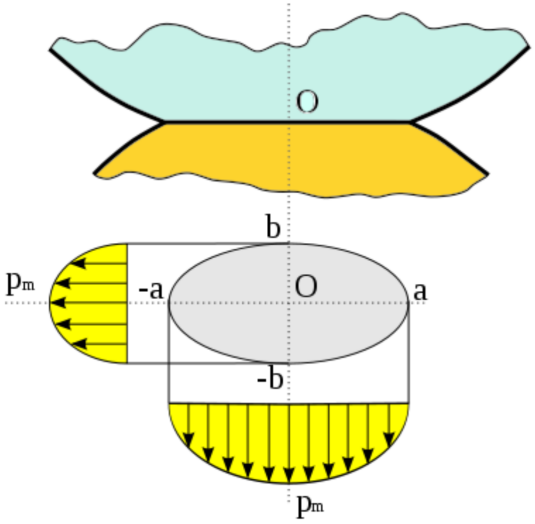


**Figure 3.1:** *Hertzian contact*

The contact stiffness depends on the material properties of both bodies in contact, through the following equation:

- Contact stiffness : $k_c = 2aE^*$
- Hertz contact radius : $a = (\frac{3LR}{4E^*})^{\frac{1}{3}}$
- Combined Young's modulus : $E^* = (\frac{1-\nu_1^2}{E_1} + \frac{1-\nu_2^2}{E_2})^{-1}$
- Combined radius of curvature : $R = (\frac{1}{R_1} + \frac{1}{R_2})^{-1}$
- Applied load : $L$
- Poisson coefficient : $\nu$
- Penetration depth : $d = (x_1 - x)$

That yields the normal force equation:

$$F = k_c(x_1 - x) = 2aE^*(x_1 - x) = \\ 2\left(\frac{3L(\frac{1}{R_1}+\frac{1}{R_2})^{-1}}{4(\frac{1-\nu_1^2}{E_1}+\frac{1-\nu_2^2}{E_2})^{-1}}\right)^{\frac{1}{3}}\left(\frac{1-\nu_1^2}{E_1} + \frac{1-\nu_2^2}{E_2}\right)^{-1}(x_1 - x) \tag{3.6}$$

MSC Adams implements the Hertzian contact logic through the IMPACT function. While the theoretical Hertzian stiffness varies with the load, Adams utilizes a constant stiffness coefficient $k$ defined by the user. The physical non-linearity of the contact is instead captured by an additional force exponent $e$, which defines the normal force as follows:

$$F = k(x_1 - x)^e \tag{3.7}$$

In this formulation, the exponent $e$ accounts for the increasing contact area during penetration, allowing a constant parameter $k$ to accurately approximate the non-linear behavior predicted by Hertz's theory. To ensure numerical stability and prevent non-physical force spikes at the moment of contact, the maximum damping value $C_{max}$ is generally defined according to the following empirical rule of thumb: $C_{max} < 0.01k$

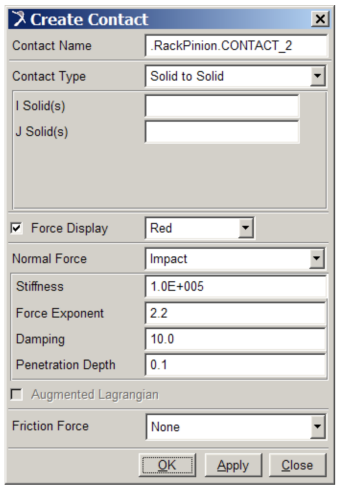


**Figure 3.2:** *MSC Adams IMPACT function specification*

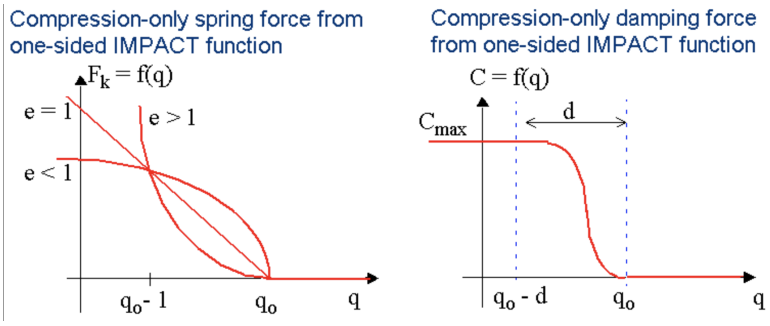


**Figure 3.3:** *MSC Adams IMPACT function representation*

## 3.3 Friction - Coulomb model

Coulomb's law of friction describes the behavior of the friction force between two bodies in contact and depends on the exchanged normal force as follows :

In order to impose a motion on a body lying on an even surface in a state of rest, a force proportional to the normal force must be applied on the body to overcome this state of rest. The force is the force of static friction, and the term of proportionality is called the *coefficient of static friction* $\mu_s$

**Static Friction**

$F_s = \mu_s F_N$

After the static force has been overcome, a resisting force $F_R$ opposes the motion. This kinetic friction force is proportional to the normal force $F_N$ through the coefficient of proportionality $\mu_k$ called the *coefficient of kinetic friction*

**Kinetic Friction**

$F_R = \mu_k F_N$

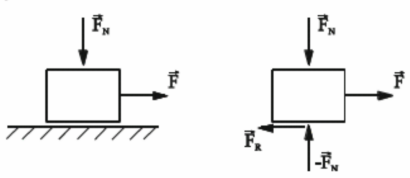


**Figure 3.4:** *Frictional force acting on a body*

As can be seen from the figure below, the behavior of the friction force causes a discontinuity in the first derivative of the friction function that cannot be solved numerically by simulation software.

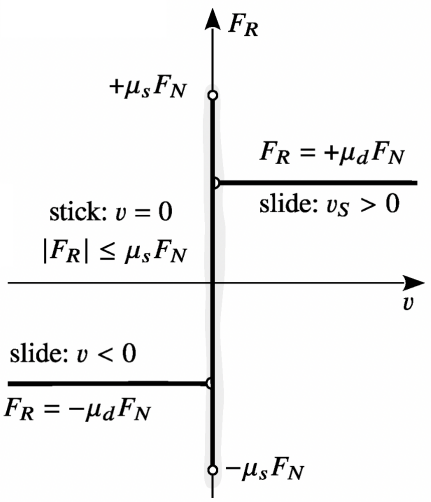


**Figure 3.5:** *Frictional force behavior*

MSC Adams models the discontinuity obtained when the value of stiction transition velocity $V_s$ approaches zero as a continuity. The function follows a cubic step function in the intervals $(-\mu_k\ ;\ -\mu_s)$, $(-\mu_s\ ;\ +\mu_s)$, and $(+\mu_s\ ;\ +\mu_k)$. In the intervals where the velocity is greater than the friction transition velocity $|V| \geq V_d$, the coefficient of friction is $\mu = \mu_d$

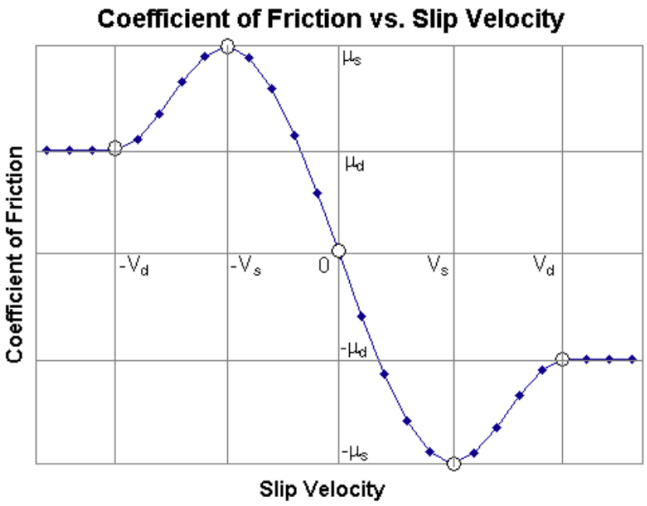


**Figure 3.6:** *Friction numerical model*

MSC Adams request $\mu_s$ , $\mu_d$ , $V_s$ , $V_d$ as input parameters for the friction model, as shown in the figure below:

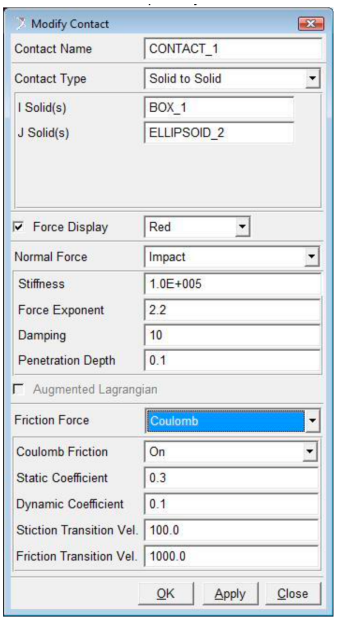


**Figure 3.7:** *MSC Adams friction force input*

Beyond the basic Coulomb implementation, MSC Adams offers the possibility to utilize a more comprehensive Stiction and Sliding formulation. This approach

enhances the friction evolution by introducing a displacement-based parameter (Maximum Stiction Deformation), ensuring a more stable transition from rest and preventing numerical 'creep' during the stiction phase.

## 3.4 Control systems - PID controller

Control systems are used whenever there's the need to manage the behavior of some physical quantities characteristic of a mechatronic system in the absence of human action, such as position, speed, torque, temperature, and so on. A control system can be divided into different characteristic blocks:

- the **plant** , a set of equations describing the system to be controlled.
- the **controlled output** $y(t)$ , the physical variables under control .
- the **control input** $u(t)$ , a manipulable variable that affects the plant.
- the **disturbance input** $d(t)$ , not manipulable variable, which affects the plant to achieve the control purpose
- the **reference signal** $r(t)$ , the prescribed values of the controlled output.
- the **controller** provides control input to the plant.

In particular, controllers can be divided into two categories:

**Open-loop controllers** (or Feedforward controllers) provide the input signal to the plant based on the past and present value of the reference signal only.

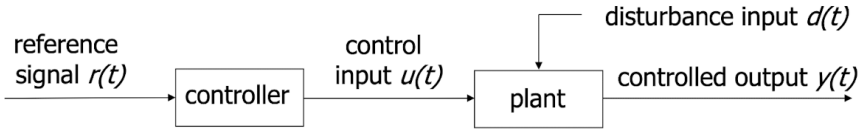


**Figure 3.8:** *Open-loop control scheme*

**Closed-loop controllers** (or Feedback controllers) provide the input signal to the plant based on past and present values of both the reference signal and, through sensors, the measured output $z(t)$

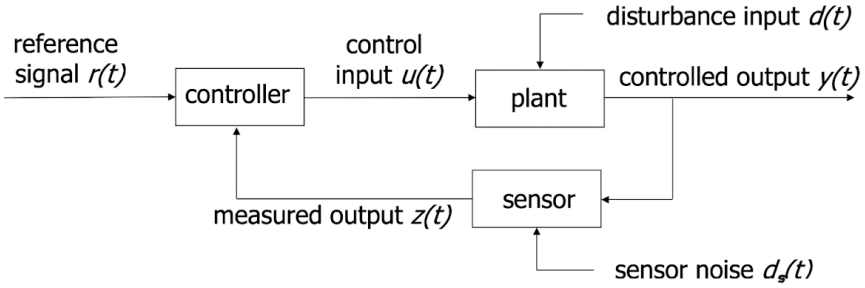


**Figure 3.9:** *Closed-loop control scheme*

Closed-loop controllers are able to reduce and compensate for the effect of the disturbances.
Usually, an **actuator** is typically included in the control scheme, its action is to convert the control action of the reference signal into the required action on the plant.

Among the various existing controllers, one of the most used is the **Proportional-Integrative-Derivative (PID) controller**[18], a linear closed-loop mechanism widely used in applications that require a continuous modulated control of the system. It uses three control terms to influence the output in order to apply an accurate control.

The characteristic equation is described below :

$$u(t) = K_p e(t) + K_i \int_0^t e(\tau)d\tau \ + K_d \frac{de(t)}{dt} \tag{3.8}$$

The PID controller continuously calculates the error value $e(t)$ as the difference between the measured output and the reference signal $e(t) = r(t) - y(t)$. The controller attempts to minimize the error by adjusting the control variable $u(t)$, applying correction based on proportional, integral, and derivative terms as shown in the figure below.

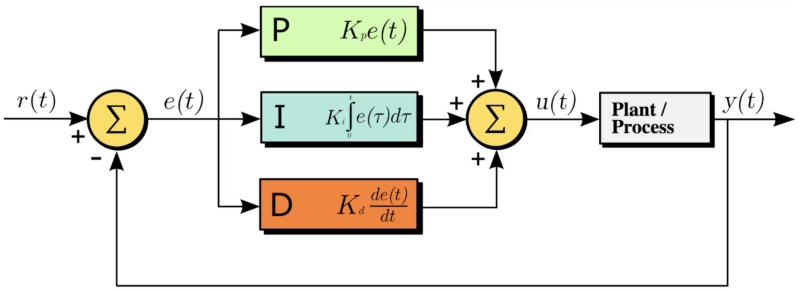


**Figure 3.10:** *PID controller scheme*

Each of the Proportional-Integrative-Derivative actions has a specific effect on the controlled system, in particular:

**Proportional term** provides a correction to the controlled variable that is proportional to the error, and so the difference between measured output and reference signal. The proportional term $P = K_p e(t)$ can be adjusted by setting the proportional gain constant.

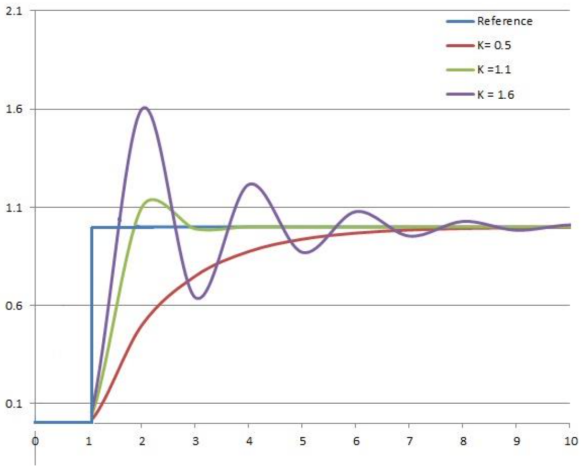


**Figure 3.11:** *Proportional term effect*

The proportional term alone is not sufficient to perform a correct control action and will result in an error between the desired final output and the actual one called steady-state error.

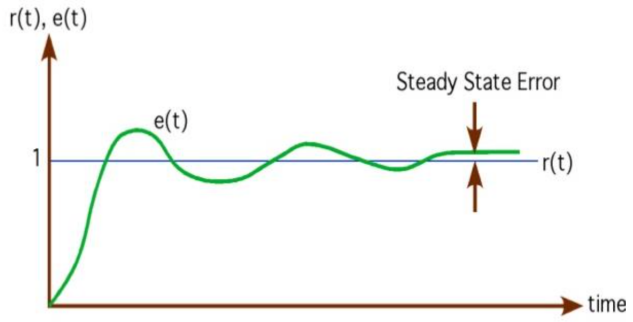


**Figure 3.12:** *Steady-state error*

**Integral term** provides a correction that is proportional to the integral of the error variable, both for magnitude and duration.
The integral term $I = K_i \int_0^t e(\tau)d\tau$ accelerates the movement of the process toward the setpoint. It eliminates the steady-state error but introduces an initial overshoot to the process variable.

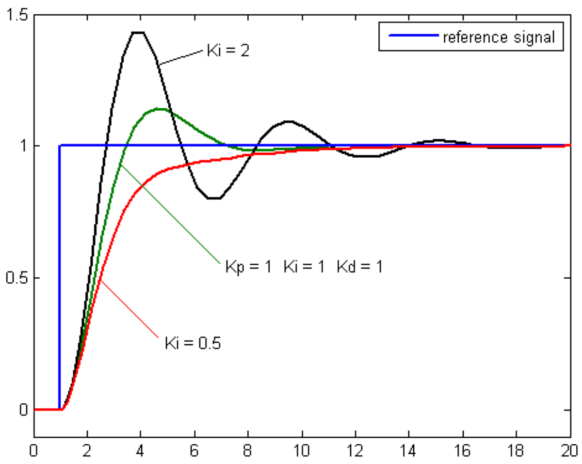


**Figure 3.13:** *Integral term effect*

**Derivative Term** provides a correction to the controlled variable that is proportional to the derivative of the error $D = K_d \frac{de(t)}{dt}$.
It corresponds to the slope of the error over time, predicts system behavior, and improves settling time and stability of the system. Derivative term is also used for overshoot reduction introduced by integral term.

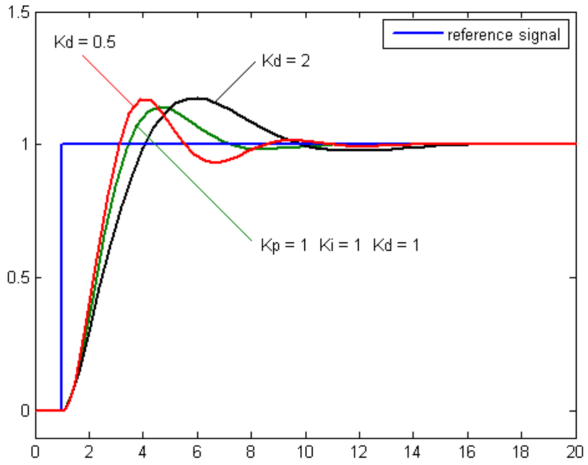


**Figure 3.14:** *Derivative term effect*

## 3.5 System engineering and trade-off analysis

NASA defines systems engineering as a multi-disciplinary approach to the design, development, technical management, operation, and retirement of a system [19]. A "system" is defined as the combination of elements that function together to produce the capability required to meet a need.

The lifecycle of a system has been standardized by system engineers as the *V-Model*, which describes the phases that a system should pass through, from the primary phases of project definition to the last phases of integration, testing, operation, and maintenance. This thesis work can be collocated in the first part of the "*V*".

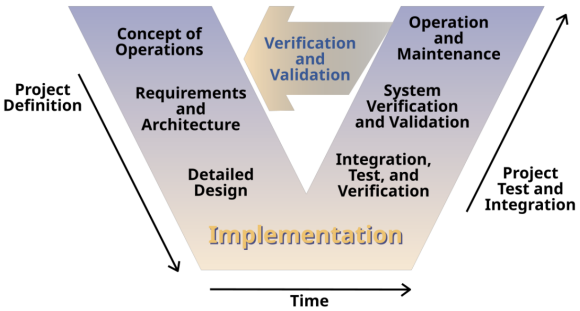


**Figure 3.15:** *V-model scheme*

System engineering also defines how to perform risk analysis, decision analysis, and trade-offs between systems. Decision analysis is a framework within which analyses of diverse types are applied to the formulation and characterization of decision alternatives that implement at best the decision-maker's priorities. The decision analysis process is depicted in Figure 3.16 :

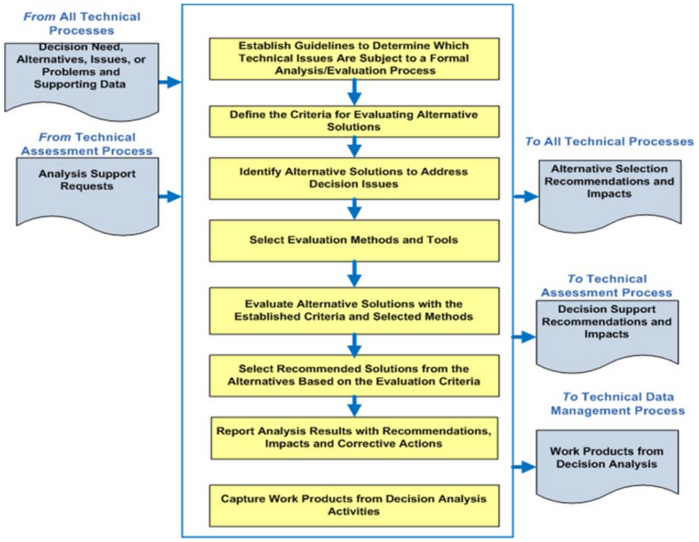


**Figure 3.16:** *Decision analysis process*

An important step for the decision analysis is the identification of alternative solutions and the definition of the criteria for evaluating alternative solutions, usually called figure of merit (FoM), in order to perform a trade-off study, which can work as an assistant to select the most suitable option for a set of viable options.

There are several methods that can support formal decision analysis, such as :

- *Influence Diagrams*
- *Decision Trees*
- *Analytic Hierarchy Process (AHP)*
- *Borda counting*
- *Utility analysis*

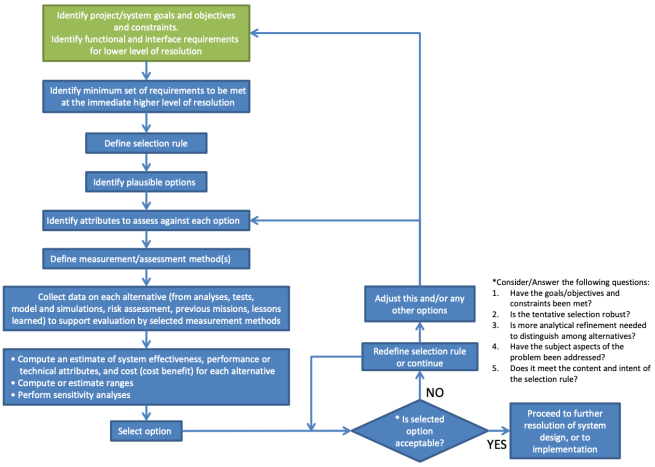


**Figure 3.17:** *Trade study process*

In particular, the method that supports this thesis work is the Analytic Hierarchy Process.

**Analytic Hierarchy Process (AHP)** is a multi-attribute methodology developed by Thomas Saaty [20], that provides an effective means to deal with complex decision-making.
It can assist the process by identifying and weighting selection criteria, analyzing collected data, helping to capture subjective and objective evaluation measures, and providing a consistency-check mechanism.
Use of AHP to determine criteria weighting is a good application of the methodology. The pair-wise comparison approach assumes all other factors are independent in the comparison. This is often not true, and the collective influence of all alternatives in the decision criteria should be considered simultaneously in these cases.
The AHP normally has six steps :

1. Describe in summary the alternatives under consideration.
2. Develop a set of high-level objectives.
3. Decompose the high-level objective from general to specific to produce an objectives hierarchy.

4. Determine the relative importance of the evaluation objectives and attributes by assigning weights arrived at by engaging experts through a structured process such as interviews or questionnaires.

5. Have each expert make pair-wise comparisons of the performance of each decision alternative with respect to a technical performance measure. Repeat this for each technical performance measure.Combine the results of these subjective evaluations mathematically using a process or, commonly, an available software tool that ranks the alternatives.

6. Iterate the interviews/questionnaires and AHP evaluation process until a consensus ranking of the alternatives is achieved.

If AHP is used only to produce the technical performance measure weights to be used in a Performance Index (PI) or Measure of Effectiveness (MOEs) calculation, then only the first four steps listed above are applicable.

# Chapter 4

# System definition and requirements

The objective of this chapter is to define the System of Interest (SoI), identified as the locomotion system of a lunar rover, and to establish the technical requirements that guide the analytical development of this research. The primary purpose of the locomotion system is to enable dexterous navigation across the lunar environment, ensuring high-performance mobility and stability for the vehicle and its payload. To fulfill these objectives, the system must be compliant with a set of requirements, which are categorized into *Mission requirements* and *System requirements*.

## 4.1 Mission requirements

As discussed in Chapter 2, several missions have studied lunar topography, establishing a historical baseline for surface operations. Recent scientific interest has focused on the lunar South Pole, particularly within the Aitken Basin and the Shackleton crater, due to the potential presence of critical resources such as water ice.

This specific operational environment imposes significant physical challenges on the locomotion system:

- Obstacle negotiation: The system must be capable of traversing unstructured

terrain with obstacles reaching a maximum height of $30cm$.

- Topographical slope: To explore crater regions, the rover must manage slope values up to 30°
- Gravitational field: All dynamic interactions are governed by a lunar gravitational acceleration of $1.62m/s^2$

## 4.2 System requirements

From a system-level perspective, requirements arise from the broader evolution of planetary robotics. As the industry moves away from large-scale, monolithic platforms toward versatile and modular designs , mid-sized rovers in the 100-150 kg range are emerging as a standard for modern exploration missions. To translate these strategic trends into a functional architecture, specific technical specifications must be established to govern the mechanical sizing and the performance targets of the mobility assembly:

- Wheel size: The requirement to negotiate $30cm$ obstacles directly dictates the geometry of the locomotion assembly. Specifically, a wheel radius $30cm$ is selected to ensure that $R \geq h_{obst.}$. This sizing is critical to allow the wheel center to pass over the obstacle crest through rolling motion, preventing mechanical locking and reducing the peak torque required from the actuators.
- Operational speed: Operating speed is a critical driver for mission efficiency. A target speed of $1m/s$ is established to guarantee significantly higher area coverage for navigation, mapping, and exploration activities compared to the capabilities of historical planetary rovers, which typically operated at much lower velocity regimes.

## 4.3 Candidate Architectures

To evaluate the impact of different kinematic configurations on the requirements established in the previous sections, four distinct architectures have been selected for comparison. To ensure a scientifically rigorous trade-off, a comparative baseline has

been defined: while the internal suspension mechanics change, the following design parameters remain invariant across all models to isolate the dynamic response of the locomotion sub-system:

- Rover Footprint: The longitudinal and lateral center-to-center distances between the wheels are kept constant. This ensures a consistent baseline for stability margins across all analyzed configurations. Based on design requirements, a footprint $1850 \times 1250mm$ has been established for all analyzed architectures.

- Core geometry and mass distribution: The main chassis (core) features identical dimensions and volume in all models. Furthermore, the Center of Mass (CoM) is maintained in the same spatial position to prevent biasing the results through varying weight distributions.

- Wheel specification: All models utilize wheels with a fixed radius $30cm$ and an identical width $30cm$, as dictated by the obstacle negotiation and soil interaction requirements. This uniformity ensures that any difference in tractive performance is due to the suspension kinematics rather than variations in wheel-soil contact geometry.

Within this fixed design envelope, the four candidate architectures represent an evolution from fully passive to fully active systems:

### 4.3.1 Rocker-Bogie [RB]

The Rocker-Bogie system is utilized as the primary flight-proven benchmark for passive stability. This architecture relies on a combination of "rocker" and "bogie" links interconnected through a differential mechanism, typically a differential bar or a gearbox. Its main strength lies in its ability to maintain all wheels in contact with uneven terrain without the need for active actuators. This mechanical configuration ensures high passive adaptability and a balanced distribution of contact forces, making it the established standard for robust obstacle negotiation in planetary exploration.

**Figure 4.1:** *RB: NASA Perseverance*

### 4.3.2 Double-Bogie [2BG]

The Double-Bogie configuration represents a simplified mechanical topology derived from traditional bogie assemblies. By utilizing two independent bogie units without a centralized differential interconnection, this model decouples the left and right suspension sides. This reduction in mechanical links aims primarily to minimize manufacturing complexity. In the context of this study, the 2B architecture serves as a critical case for evaluating the efficiency of skid-steering maneuvers. The absence of complex passive linkages provides a clearer perspective on the vehicle's dynamic response during high-speed transit

**Figure 4.2:** *2BG: LeoRover*

### 4.3.3 Four Wheel Active [4WA]

Representing a shift toward mechatronic-driven mobility, the Four-Wheel Active architecture completely replaces traditional passive linkages with independent active suspension units. This system draws inspiration from the design philosophy of state-of-the-art planetary platforms, such as NASA's VIPER rover, and high-performance research prototypes like the AMALIA rover, developed by the DIANA student team of Politecnico di Torino.

The primary advantage of the 4WA configuration is its ability to actively shift the vehicle's Center of Mass (CoM) relative to the wheels. This capability is critical for maintaining traction on the steep 30° slopes defined in the mission requirements, as the system can compensate for weight transfer to prevent wheel stall or soil failure. Furthermore, the active control of each suspension arm allows the rover to "climb" over the 30*cm* obstacles through coordinated movement, rather than relying on the passive compliance of the frame, offering a high degree of agility in the unstructured terrain.

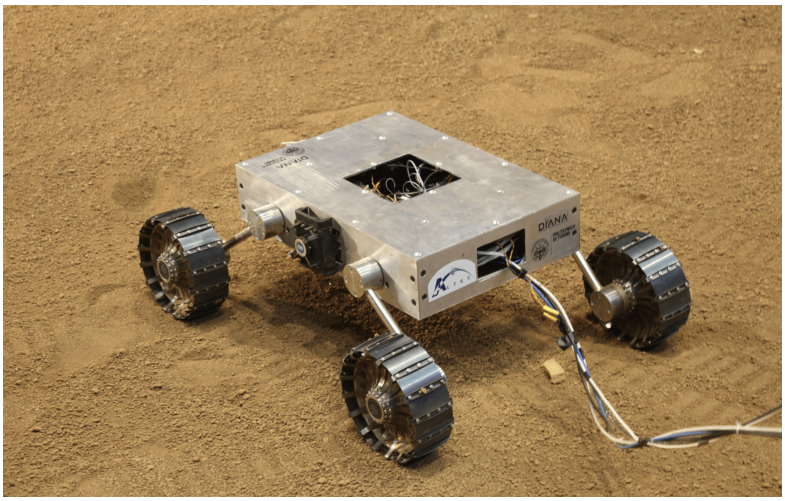


**Figure 4.3:** *4WA: Team DIANA AMALIA*

### 4.3.4 Hybrid [HBD]

The Hybrid model is designed as a multimodal platform, characterized by an articulated wheeled configuration. Drawing inspiration from the design philosophy

of NASA's ATHLETE (All-Terrain Hex-Legged Extra-Terrestrial Explorer) rover, this architecture incorporates additional active joints that allow the vehicle to implement different operating modes depending on the terrain conditions.

In particular, the HBD system is capable of performing a walking gait by coordinating its articulated segments and locking wheel rotation when necessary. This multimodal capability provides a significant advantage in navigating the most challenging areas of the lunar surface, allowing the rover to overcome geometric obstacles or low-traction zones that would otherwise limit the performance of a standard wheeled vehicle.

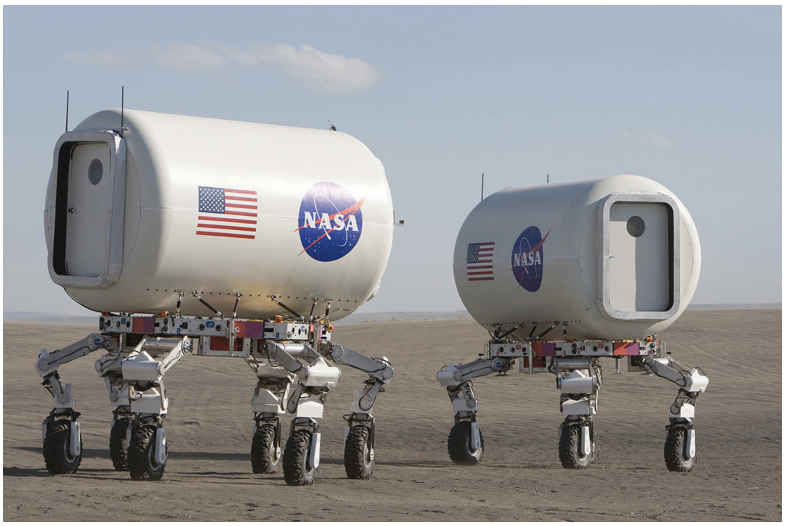


**Figure 4.4:** *HBD: NASA ATHLETE*

## 4.4 Summary of System Requirements

The following table summarizes the requirements and target specifications for the locomotion system analyzed in this work. These parameters serve as the benchmarks for evaluating the candidate architectures.

**Table 4.1:** *Requirements summary*

| Requirement | Target value | Description |
|---|---|---|
| **Operational speed** | $1 m/s$ | The locomotion system shall enable a steady-state velocity of 1.0 m/s on flat terrain. |
| **Mass budget** | $100 \div 150 kg$ | The total mass of the rover platform shall not exceed 150 kg. |
| **Obstacle negotiation** | $30 cm$ | The system shall be capable of overcoming obstacles of 30 cm |
| **Climbing performance** | $\pm 30°$ | The locomotion system shall maintain traction and stability on longitudinal slopes up to 30 degrees. |
| **Wheel sizing** | $30 cm$ | The wheel radius shall be at least 30 cm to ensure compliance with the target obstacle height. |
| **Environmental gravity** | $1.62 m/s^2$ | The system design shall be optimized for the lunar gravitational acceleration. |
| **Design invariants** | *constant* | All candidate architectures shall share identical center-to-center wheel distances and dimensions, core mass, dimensions, and initial position for comparative validity. |

The numerical values of the selected design invariants are presented in the table below:

**Table 4.2:** *Design invariants value*

| Parameter | Value | Description |
|---|---|---|
| **Longitudinal footprint** | $1850mm$ | Center-to-center distance between the wheels (length) |
| **Lateral footprint** | $1250mm$ | Center-to-center distance between the wheels (width) |
| **Core dimension** | $750 \times 750 \times 30mm$ | External dimensions of the core structure ($L \times W \times H$) |
| **Core mass** | $86kg$ | Fixed mass of the core |
| **Core's CoM location** | $870mm$ | Height of the core CoM from the ground. |

The detailed mass budget for the core mass is:

- Payload $25kg$
- Batteries $50kg$
- Avionics $10kg$
- Structure $1kg$

In particular, the mass of the batteries is estimated by taking into consideration that the rover must survive 100 hours of the lunar night, assuming an energy consumption adequate to the activities to be performed. The mass of avionics is estimated considering harnessing and electronic boards, including radiation hardening layers.

# Chapter 5

# Mission Scenarios and Performance Metrics

The objective of this chapter is to define the analytical framework used to evaluate and compare the four candidate locomotion architectures. By leveraging the MSC Adams multibody environment, a series of standardized virtual testbeds have been developed to transform the formal system requirements into quantifiable performance data

## 5.1 Design Reference Missions (DRMs)

To ensure a consistent baseline for comparison, all DRMs share core simulation parameters. These include a lunar gravitational acceleration $1.62 m/s^2$ and a wheel-soil contact model based on the MSC Adams IMPACT function.

To prevent the solid-to-solid contact from producing unrealistic force spikes or divergent dynamic behavior, all geometric edges of the terrain and obstacles in the first two DRMs were filleted and smoothed. This ensures that the solver maintains a coherent and stable response throughout the simulation.

### 5.1.1 DRM1 Slope climbing

As shown in Figure 5.1, this environment consists of a continuous track with different height levels. The path starts with a flat section to allow the rover to reach a steady state before hitting a 30° upward slope. This is followed by a 1000$mm$ long, flat plateau.The second part of the mission features a 35° downward slope. This section is designed as an "off-nominal" test, as it exceeds the 30° requirement set for the project. The goal is to see how the different suspension systems behave in critical climbing conditions.

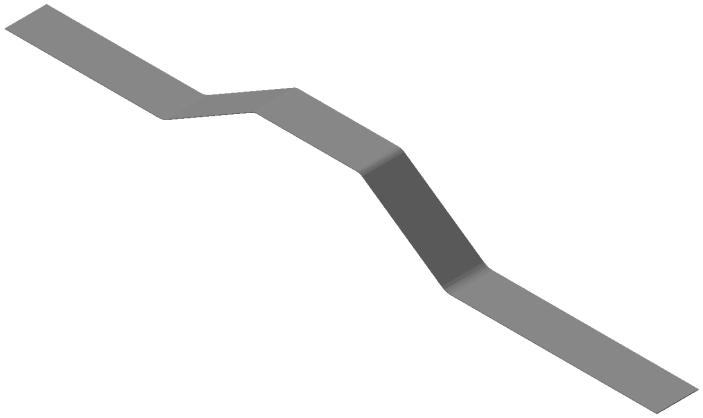

**Figure 5.1:** *Slope*

### 5.1.2 DRM2 Obstacle overcoming

As shown in Figure 5.2, the environment for this mission is a straight track 30 m long and 3 m wide. It is designed to evaluate the rover's capability to negotiate uneven terrain through a sequence of discrete obstacles. The track features a series of blocks with heights of 100 mm, 200 mm, and 300 mm . These are arranged in an alternating pattern to ensure that only one side of the locomotion system is engaged at a time. This specific layout tests the suspension's ability to articulate independently and maintain a stable, horizontal core attitude while traversing asymmetric hazards. The sequence includes a 400 mm obstacle. This height exceeds the 300 mm project requirement and serves to identify the mechanical and control limits of the candidate architectures when facing extreme topographical discontinuities.

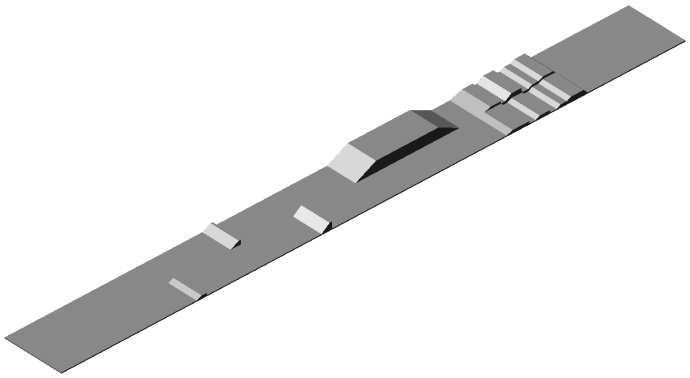

**Figure 5.2:** *Obstacles path*

### 5.1.3 DRM3 Steering capabilities

The third environment, shown in Figure 5.3, is a large, flat platform measuring $2700 \times 2500\,\text{cm}$ . There are no vertical obstacles or slopes in the field. This flat area allows the rover to perform circular paths at its target speed of $1\,\text{m/s}$. The simplicity of the ground ensures that any instability is strictly due to the steering mechanics (like the friction of skid-steering) rather than terrain irregularities.

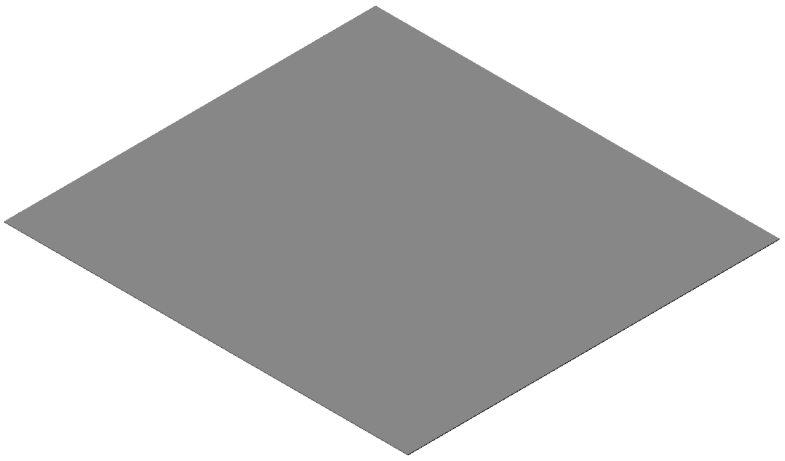

**Figure 5.3:** *Steering platform*

## 5.2 Figures of Merit (FoMs)

Performance is quantified using Figures of Merit (FoMs), which translate raw simulation data into a comparable format for the final trade-off analysis. These metrics are grouped into architectural properties and dynamic responses.

### 5.2.1 Architectural static metrics

These parameters are evaluated independently of the mission environment to assess the physical impact of each design:

- **Total mass**: While core and wheel masses are invariant for all models, the total mass varies according to the specific suspension links and motors required by each architecture.
- **Complexity**: A metric quantifying the design and integration effort, divided into point of failure, structural complexity, number of actuators, and control complexity. Complexity is set as a critical figure of merit for a space project, as from complexity, badly dealt with, can come unreliability and higher costs. It has been evaluated based on pairwise comparison matrices based on the following consideration:
  - Point of failures: Is the pairwise comparison between mobilities intrinsic magnitude of the point of failures number. The score measures the complexity in terms of the number of component types representing single points of failure.
  - Structure: Is the pairwise comparison between mobilities, structural load magnitude, and predictability related to structure complexity. It addresses the geometry, the steering capability, and the linearity of load evolution during traverse.
  - Actuators number: Is the pairwise comparison between actuators number. The score is computed by linearizing and ceiling the number of actuators difference between the four architectures.
  - Control complexity: Is the pairwise comparison of the software and algorithmic effort needed to operate the rover. The score ranges from simple

traction management to complex, high-frequency Inverse Kinematics. This metric evaluates the system's capability to handle coordinated steering, correct for wheel slippage, and use real-time data to adapt the rover's posture to uneven terrain.

The AHP method has been used as the complexity problem is easily analyzed by comparing the different design solutions in pairs. The score is defined in Chapter 7.

### 5.2.2 Global dynamic FoMs

Calculated using the same mathematical approach across all DRMs:

- **Speed and slip stability**: The dynamic limits of the rover are evaluated through its capacity to maintain stability and prescribed trajectory while managing lateral drift effects or bumps. In the lunar environment, the primary operational constraint during high-speed maneuvers is the loss of directional control, which occurs when side-slip forces or unbalanced contact with soil exceed the available friction between the wheels and the terrain. The methodology identifies the critical velocity $v_{crit}$ as the threshold beyond which the rover significantly deviates from the target path due to drift.

- **Power consumption**: To ensure a comparison between passive and active systems, power consumption in general is modeled as the total electrical power ($P_{el}$) that accounts for mechanical power ($P_{mech}$) in moving joints for $\omega \neq 0$, and Joule heating losses ($P_{hold}$) both for moving joints and active control joints that maintain the rover's attitude under stall conditions with $\omega = 0$. To simulate a conservative worst-case scenario, the mechanical power is calculated using the absolute value of torque and angular velocity. This approach purposefully disregards any potential regenerative braking effects, assuming all energy required for braking or speed control is dissipated rather than recovered.

  For each motor $i$, the total power consumption across the simulation timespan is defined as

$$P_{el_i}(t) = P_{mech_i}(t) + P_{hold_i}(t) = \tau_i \cdot \omega_i + R \cdot (\frac{\tau_i}{K_t})^2 \tag{5.1}$$

Where:

- $P_{mech} = \tau_i \cdot \omega_i$ is the mechanical power spent to move joints, is computed as the product of torque and angular velocity.
- $P_{hold} = R \cdot (\frac{\tau_i}{K_t})^2$is the power dissipated as heat. Where $R$ is the winding resistance, and $K_t$ is the torque constant, derived from the selection of a representative motor from commercial catalogs (e.g., Maxon , Moog) that meets the torque requirements.

For trade-off analysis, two metrics are derived:
**Mean Power consumption**, averaged over the simulation timespan,

$$P_{mean} = \frac{1}{N} \sum_{k=1}^{N} P(t_k) \tag{5.2}$$

and **Peak Power consumption**, the maximum instantaneous electrical power recorded during the entire simulation:

$$P_{peak} = \max_{t_k} |P_{el}(t_k)| \tag{5.3}$$

- **Stability index**: Dynamic stability is evaluated through the Root Mean Square (RMS) values of triaxial acceleration values, measured at a specific marker in rover models, placed $50cm$ above the Core Center of Mass (CoM) to account for the effect that payloads and instruments could suffer during a traverse in a specific environment. The values are computed for all the simulation timespans as follows:

$$a_{RMS} = \sqrt{\frac{1}{N} \sum_{k=1}^{N} |a(t_k)|^2} \tag{5.4}$$

where, at each time instant $t_k$, the acceleration value is $|a(t_k)| = \sqrt{a_x^2 + a_y^2 + a_z^2}$

- **Angular stability index**: Introduced to complement the translational stability analysis, this metric evaluates the angular posture of the architectures. For DRM1, it accounts for pitch angle stability by calculating the RMS value of the pitch angle $\theta_{pitch,RMS}$ as the platform traverses a slope. For DRM2, the same metric evaluates roll angle stability $\theta_{roll,RMS}$, reflecting the rover's response to the arrangement of obstacles along the path.

- **Maximum operational velocity**: identifies the upper boundary of the rover's performance envelope. It is defined as the maximum steady-state speed achievable before the system encounters a dynamic failure mode.

### 5.2.3 Scenario-specific metrics (DRM3)

While power and stability are global indicators, the steering maneuver in DRM3 requires specific metrics to evaluate the agility and controllability of each architecture:

- **Minimum steering radius**: This metric defines the architecture agility limit. For each model, a series of simulations is conducted with decreasing values of *steering radius* $R$. The minimum radius is identified at the value at which the rover can still complete a full 360° turn without experiencing loss of traction.
- **Path following and position error**: Control precision is evaluated by the system's ability to match a target circular trajectory of radius $R_{target}$. To isolate the steering behavior, the position error is monitored using the radial error $\Delta\rho$ defined as follows:

$$\Delta\rho = \rho(t) - R_{target} \tag{5.5}$$

  However, due to the physics of lateral scrubbing, some architectures require a theoretical command radius ($R_{th}$) significantly larger than the desired trajectory. To quantify this discrepancy, a steering command gain ($G_R$) is introduced :

$$G_R = \frac{R_{th}}{R_{target}} \tag{5.6}$$

  Values of $G_R$ are expected to be $G_R \approx 1$ for explicit steering systems, while values of $G_R > 1$ are expected for skid-steering ones. $G_R$ will be utilized as a weighting factor in the final trade-off analysis to penalize architectures characterized by high command saturation and kinematic inefficiency.

To provide a comprehensive overview of the comparative logic, the flowchart below synthesizes the transition from architectural selection to the extraction of

the figures of merit. This map clarifies how each metric contributes to the final decision-making process.

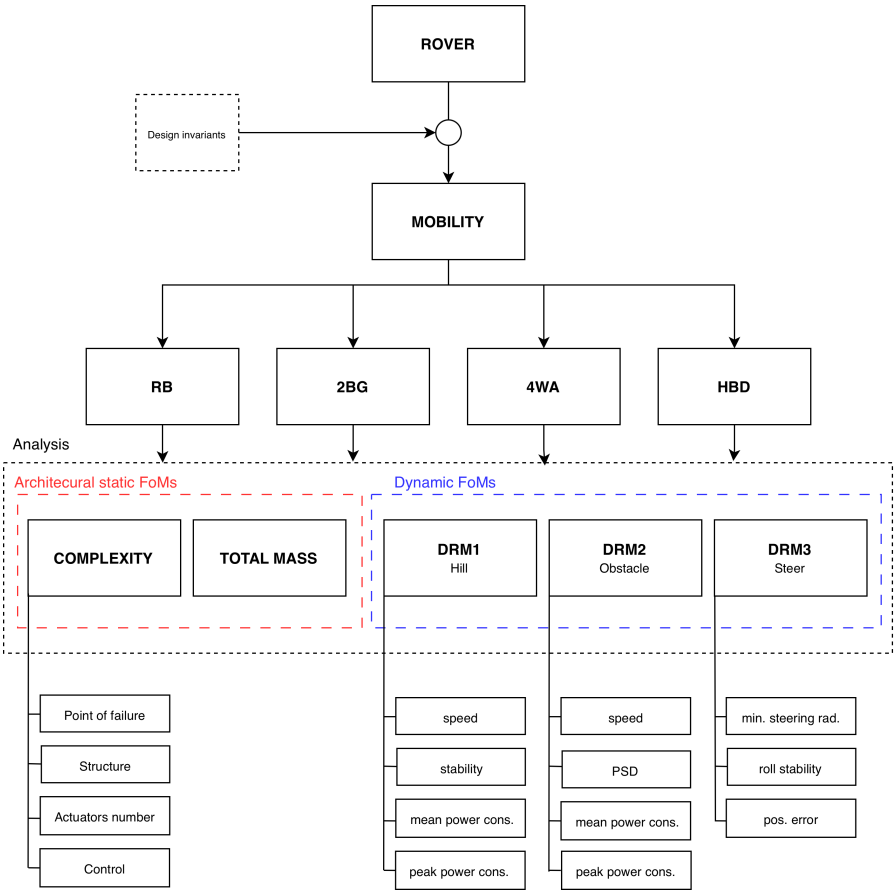


**Figure 5.4:** *System workflow*

# Chapter 6

# Multibody modeling

The development of the multibody models originates from the mission requirements, which directly influence the technical specifications of the components and the inertial properties that must be accurately defined in MSC Adams to ensure the fidelity of the dynamic simulations.
To ensure clarity and conciseness in the following descriptions, all inertial properties are presented according to the standard symmetric inertia tensor matrix **I**. For each component, values are calculated relative to its Center of Mass (CoM) following this symbolic structure:

$$\mathbf{I} = \begin{bmatrix} I_{xx} & I_{xy} & I_{xz} \\ I_{xy} & I_{yy} & I_{yz} \\ I_{xz} & I_{yz} & I_{zz} \end{bmatrix} \quad [\mathrm{kg} \cdot \mathrm{mm}^2]$$

The subsequent sections detail the methodological workflow that transitions from the initial mission requirements to the development of simulation-ready multibody models.

## 6.1 Modeling workflow

While the MSC Adams environment allows for the direct implementation of complex geometries and kinematic calculations through its native tools, a multi-software approach was adopted in this study. The integration of external CAD models

ensured greater precision in the mass budget definition, while the use of MATLAB for deriving the steering kinematic equations and angle constraints provided superior flexibility in the modeling and refinement phases.
The first step of the process involved the definition of the invariant components, equal for different models. In particular:

**Core** has been designed starting from a detailed mass budget. The approach accounts for internal subsystems that are not explicitly modeled as separate rigid bodies in the simulation but whose mass significantly influences the rover's inertial properties.
The core's volumetric dimensions were established through proportional ratios derived from the rover's ground footprint. The resulting CAD model is illustrated in Figure 6.1.

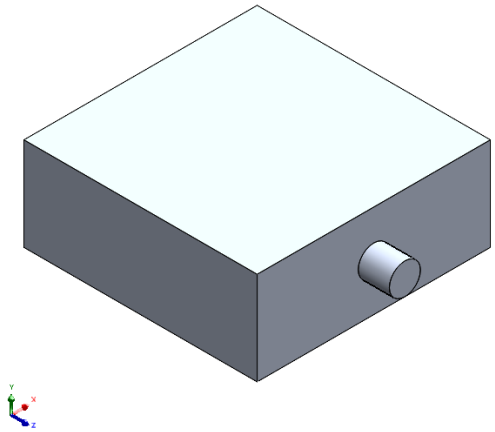

**Figure 6.1:** *Rover's core*

Core mass was estimated based on the following breakdown:

- Payload $25kg$
- Batteries $50kg$
- Avionics $10kg$
- Structure $1kg$

Reaching a total mass of $\mathbf{M_{core} = 86kg}$.

To ensure simulation fidelity, the resulting mass value has been manually overridden onto the core's representative CAD, obtaining the reference inertia matrix of the component . This allowed the solver to treat the core as a single rigid body with the correct total weight and balanced inertia, accurately reflecting the internal distribution of hardware.

Core's inertia matrix used in the architecture model is :

$$\mathbf{I} = \begin{bmatrix} 4.77 \times 10^6 & I_{xy} & I_{xz} \\ 0 & 8.13 \times 10^6 & I_{yz} \\ 0 & 0 & 4.63 \times 10^6 \end{bmatrix} \ [\text{kg} \cdot \text{mm}^2]$$

**Wheels** serve as the fundamental interface between the vehicle and the lunar surface. To ensure consistency across the different architectures, a standard geometry with a radius of $300mm$, as prescribed by the requirement, and width of $300mm$ was adopted. Since the detailed design of space-grade wheel treads is not the primary focus of this research, these components were modeled as simplified rigid bodies.

The reference material selected is **AISI-304** stainless steel. This choice is specifically motivated by the need to withstand the high abrasiveness of the lunar regolith, ensuring adequate wear resistance and mechanical durability throughout the mission's operational life.

The CAD where inertial values have been deducted is shown in Figure 6.2:

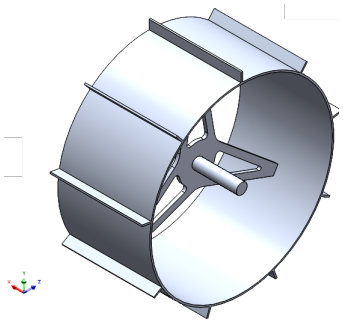

**Figure 6.2:** *Rover's Wheel*

The mass of each wheel, equal to $\mathbf{M_{wheel} = 7kg}$, and the corresponding inertial properties were extracted directly from the CAD model by assigning the physical

properties of the chosen material. Wheel's inertia values are:

$$\mathbf{I} = \begin{bmatrix} 5.3 \times 10^5 & I_{xy} & I_{xz} \\ 0 & 3.1 \times 10^5 & I_{yz} \\ 0 & 0 & 3.1 \times 10^5 \end{bmatrix} \ [\mathrm{kg} \cdot \mathrm{mm}^2]$$

## 6.2 Candidate Architectures Implementation

Once the invariant components, the core and the wheels, have been defined, the modeling workflow proceeds with the synthesis of the four candidate architectures. In this phase, the common elements are interconnected through specific structural links and kinematic pairs that define the mechanical identity of each rover.

The following sections describe the unique features of each model, focusing on the inertial properties of the specific links of each architecture and the topology of the joints that govern the locomotion performance. The material selected for structural links is **Al-6061 T6** aluminum alloy.

### 6.2.1 Rocker-Bogie model [RB]

The Rocker-Bogie architecture, characterized by the mechanical advantages discussed in Chapter 4, focuses on the integration of its characteristic suspension links with the invariant core and wheel assemblies. The assembly process is designed to accurately map the system's specific mass distribution and define the internal degrees of freedom that characterize its kinematic chain.

#### Specific Links and Inertial Properties

The architecture-specific assembly is composed of two primary links: the Rocker and the Bogie. Mass properties of the links are extracted from CAD considering the specified material, obtaining $\mathbf{M_{rocker}} = \mathbf{1.9kg}$ and $\mathbf{M_{bogie}} = \mathbf{1.1kg}$. The components are shown in Figure 6.3

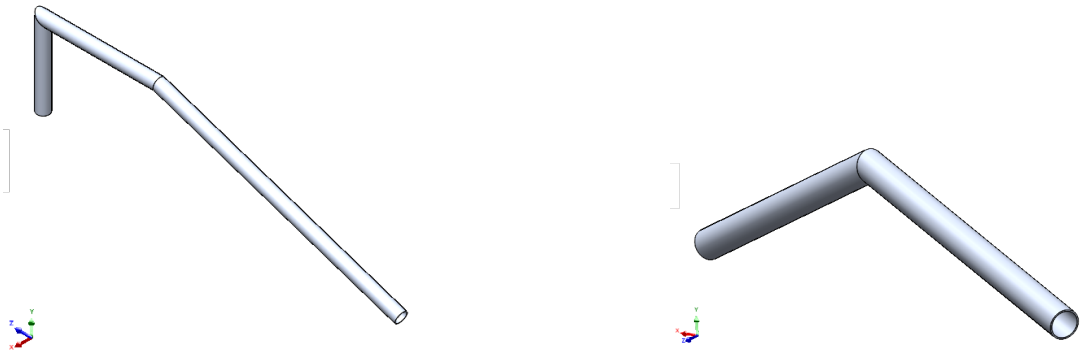

**Figure 6.3:** *Rocker (left) and Bogie (right)*

Respectively, inertia matrix are:

$$\mathbf{I_{rocker}} = \begin{bmatrix} 4.7 \times 10^5 & I_{xy} & I_{xz} \\ -0.86 & 4.5 \times 10^5 & I_{yz} \\ -3.42 & 6.3 \times 10^4 & 2.5 \times 10^4 \end{bmatrix} \ [\text{kg} \cdot \text{mm}^2]$$

and:

$$\mathbf{I_{bogie}} = \begin{bmatrix} 9.4 \times 10^4 & I_{xy} & I_{xz} \\ -0.45 & 7.6 \times 10^4 & I_{yz} \\ -0.83 & 3.4 \times 10^4 & 1.94 \times 10^4 \end{bmatrix} \ [\text{kg} \cdot \text{mm}^2]$$

### Assembly and Kinematic Topology

The connectivity of the system is realized through a series of revolute joints that enable the characteristic passive pivoting of the suspension. To facilitate a clear technical inspection of the assembly, the model is illustrated in Figure 6.4 using a half-rover view. This visual approach isolates the primary kinematic chain, highlighting the specific interconnections between the suspension links, the core, and the wheels without the visual redundancy of the symmetrical components.

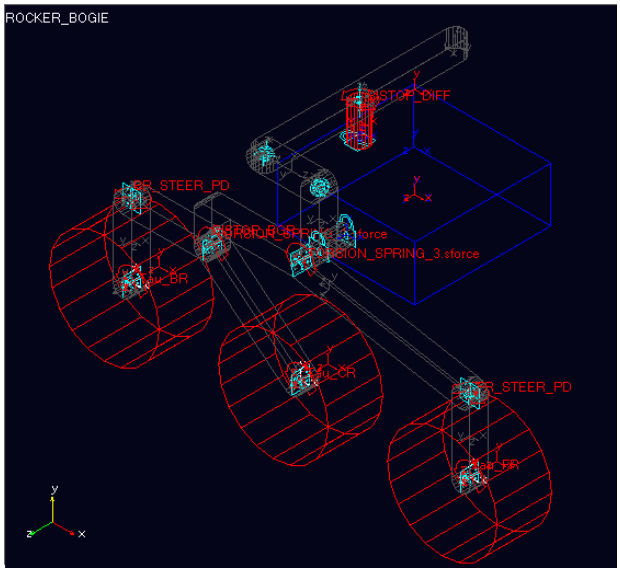


**Figure 6.4:** *RB model topology*

Building on this visual layout, the joint topology for the entire multibody model is formalized in the table below. The table maps the connections observed in the half-rover view to the complete set of constraints required for the full-vehicle simulation, specifying the total quantity of joints used in the assembly.

**Table 6.1:** *RB model topology specifications*

| **ID** | **Joint type** | **Body 1** | **Body 2** |
|---|---|---|---|
| J1 | Fixed | Core | Connector |
| J2 | Revolute | Connector | Rocker |
| J3 | Fixed | Rocker | Differential sys. link 1 |
| J4 | Revolute | Rocker | Front steer |
| J5 | Revolute | Rocker | Bogie |
| J6 | Revolute | Bogie | Back steer |
| J7 | Revolute | Bogie | Central wheel |
| J8 | Revolute | Back steer | Back wheel |
| J9 | Revolute | Front steer | Front wheel |
| J10 | Spherical | Differential sys. link 1 | Differential sys. link 2 |
| J11 | Spherical | Differential sys. link 2 | Differential bar |
| J12 | Revolute | Differential bar | Differential sys. hinge |
| J13 | Fixed | Differential sys. hinge | Core |

To capture the physical behavior of a real-world assembly and ensure numerical

stability during simulation, the theoretical kinematic model was refined with the addition of compliant and limiting elements.

Following the joint definitions, the following force-based components were integrated:

- **Rotational Spring-Damper**:Added to account for the compliance behavior of passive joints, it has been applied to joints **J2** and **J5**. Considering the chosen values, it allows the body to rotate freely around the mentioned joint:
  $K_{spring} = 100N \cdot mm/deg$
  $C_{damp} = K \cdot 1E-03N \cdot mm \cdot s/deg$

- **Mechanical Hard-Stops**: Used to account for the maximum angular excursion of the rocker through a constraint on the differential system's bar rotation of $\pm 5°$, and the bogie through a constraint on the rotation around **J5** of $\pm 25°$. In particular, the equation, defined as a torque through a Two-sided impact function, is expressed as follows:

$$BISTOP(\theta_{J5}, \omega_{J5}, \theta_{lim_1}, \theta_{lim_2}, K, e, C, Ramp) \tag{6.1}$$

  Where $K, e, C$ are the characteristic values of the impact function as explained in the Hertz theory section and $\theta_{lim_{1,2}}$ represent the upper and lower trigger values.

### Actuation Setup

The final stage of the Rocker-Bogie modeling involves the definition of the active components responsible for locomotion. Consistent with the architectural design, the model is equipped with six traction motors, applied on the wheels in joints **J9**, **J7**, and **J8** (and their symmetrical counterparts), and four steering motors, applied on joints **J4** and **J6** (and their symmetrical counterparts). The control architecture is organized into a high-level kinematic logic that defines the movement requirements and a low-level dynamic actuation that translates these requirements into motor torques and targets:

**Steering Logic** : To define the reference values for maneuvers involving directional changes, such as those required in DRM3 for steering performance evaluation, a kinematic command logic is implemented. This logic computes the target setpoints for both steering angles ($\theta_{target}$) and wheel angular velocities ($\omega_{target}$) based on the desired trajectory. To compute the required values, the **Double Ackermann** [21] steering geometry is adopted. This model ensures that all wheels rotate around a common Instantaneous Center of Rotation (ICR), minimizing tire scrubbing and energy dissipation. Given a target turning radius $R_{st}$ and the longitudinal wheelbase $L$, the fundamental governing equations for the steering angles of the corner wheels are:

$$\theta_{target,i} = \arctan\left(\frac{L/2}{R_{st} \pm w/2}\right) \tag{6.2}$$

To ensure pure rolling motion without slippage, the angular velocity of each wheel must be proportional to its distance from the Instantaneous Center of Rotation (ICR). Once the desired velocity of the rover's center of mass ($V_{cm_{des}}$) and the target turning radius ($R_{st}$) are defined, the angular velocity of the rover system about the ICR is given by $\Omega = V_{cm_{des}}/R_{st}$.
Consequently, the target angular velocity for the i-th wheel ($\omega_{target,i}$) is calculated based on its lateral distance from the ICR:

$$\omega_{target,i} = \frac{\Omega \cdot (R_{st} \pm w/2)}{R_{wheel}} = \frac{V_{cm_{des}}}{R_{st}} \cdot \frac{R_{st} \pm w/2}{R_{wheel}} \tag{6.3}$$

Where:

- $R_{wheel}$ is the wheel radius.
- $R \pm w/2$ represents the lateral distance from the ICR to the wheel's longitudinal axis (inner or outer side).

This simplified formulation is kinematically consistent for all wheels on the same side: while the corner wheels travel along a larger circumference, their steering angle compensates for this, resulting in a required traction velocity that depends only on the lateral offset from the rover's midline.

To automate the calculation of these setpoints for different maneuvers, the kinematic relations were implemented in a MATLAB script. This allowed for a

rapid generation of the input functions required by the MSC Adams solver, as shown in the following snippet:

```
% Rover Parameter Definitions
L = 1850;           % [mm] Total length (front-to-rear axis)
W = 1250;           % [mm] Lateral track width
R_wheel = 300;      % [mm] Wheel radius

% Target Parameters (from DRM)
V_cm_des = 1000;    % [mm/s] Desired rover CoM velocity
Radius = 1.15e4;    % [mm] Target turning radius

% Calculations
% 1. Angular velocity of the virtual center axis
omega_rover = V_cm_des / Radius;

% 2. Velocities for CENTRAL wheels
v_CR = omega_rover * (Radius - W/2); % Inner side (Right)
v_CL = omega_rover * (Radius + W/2); % Outer side (Left)

omega_target_CR = v_CR / R_wheel;    % [rad/s]
omega_target_CL = v_CL / R_wheel;    % [rad/s]

% 3. Velocities for FRONT & REAR steering wheels
R_int_steer = sqrt((Radius - W/2)^2 + (L/2)^2); % Inner radius
R_ext_steer = sqrt((Radius + W/2)^2 + (L/2)^2); % Outer radius

v_FR_BR = omega_rover * R_int_steer; % Front/Rear Inner
v_FL_BL = omega_rover * R_ext_steer; % Front/Rear Outer

omega_target_FR_BR = v_FR_BR / R_wheel; % [rad/s]
omega_target_FL_BL = v_FL_BL / R_wheel; % [rad/s]

% 4. Ackermann steering angles (Front/Rear wheels)
phi_i = atan((L/2) / (Radius - W/2));   % [rad]
phi_o = atan((L/2) / (Radius + W/2));   % [rad]
```

**Listing 6.1:** Rocker-Bogie 6-Wheel Ackermann kinematic calculation

**Steering Torque** :

$$\tau_{steer,i} = -K_{P_{st}} \cdot (\theta_{J,i,measured} - \theta_{target}) - K_{D_{st}} \cdot \omega_{J,i,measured} \tag{6.4}$$

Where $K_{P_{st}}$ and $K_{D_{st}}$ are the proportional and derivative gains, respectively, tuned to achieve the desired response time and damping. The value of $\theta_{target}$ changes according to the specific maneuver required by the DRM.

**Traction Torque** :

$$\tau_{trac} = R_{wheel} \cdot F_{c,yi} \cdot sin(\theta_{pitch}) + G_{\tau} \cdot (1 - \frac{\omega_{measured}}{\omega_{target}}) \tag{6.5}$$

This is a PD-based torque equation in which some correction factors were applied, taking into account the presence of soil and the change of load on the wheels according to ground inclination. In particular, these terms are

- Wheel radius $R_{wheel}$
- Normal contact force on the i-th wheel $F_{c,yi}$, allowing for dynamic load distribution.
- Pitch inclination $\theta_{pitch}$ measured relative to the rover's core to compensate for gravitational resistance
- Slippage correction factor, which accounts for the wheel-soil interaction as a function of the static friction coefficient $G_{\tau} = p\% \cdot \mu_s$
- measured and target value of wheels angular velocity ($\omega_{target}$,$\omega_{measured}$), selected to obtain the target cruise velocity of the rover

### 6.2.2 Double-Bogie model [2BG]

The Double-Bogie architecture represents a four-wheeled configuration where the load is distributed through two pivoting bogies. Unlike a completely independent suspension, these elements are mechanically coupled to the core via a differential system to maintain stability during traversal.

### Specific Links and Inertial Properties

The assembly is composed of a unique element shown in Figure 6.5 that links together the core, wheels, and differential system. As with other structural components, the material assigned to the part is **Al-6061 T6** aluminum alloy, obtaining a $\mathbf{M_{bogie} = 1.9kg}$.

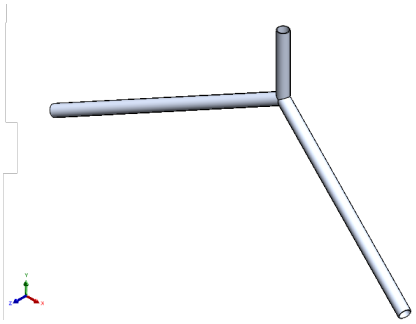

**Figure 6.5:** *2BG structure*

The inertia matrix of the element is:

$$\mathbf{I} = \begin{bmatrix} 7.16 \times 10^4 & I_{xy} & I_{xz} \\ -3.95 & 5.5 \times 10^5 & I_{yz} \\ -3.34 & -2.8 \times 10^4 & 5.9 \times 10^5 \end{bmatrix} \quad [\text{kg} \cdot \text{mm}^2]$$

### Assembly and Kinematic Topology

The differential system of the model follows the same kinematic chain as Rocker-Bogie's , while the Double-Bogie's structure rigidly rotates around a single joint attached to the core.

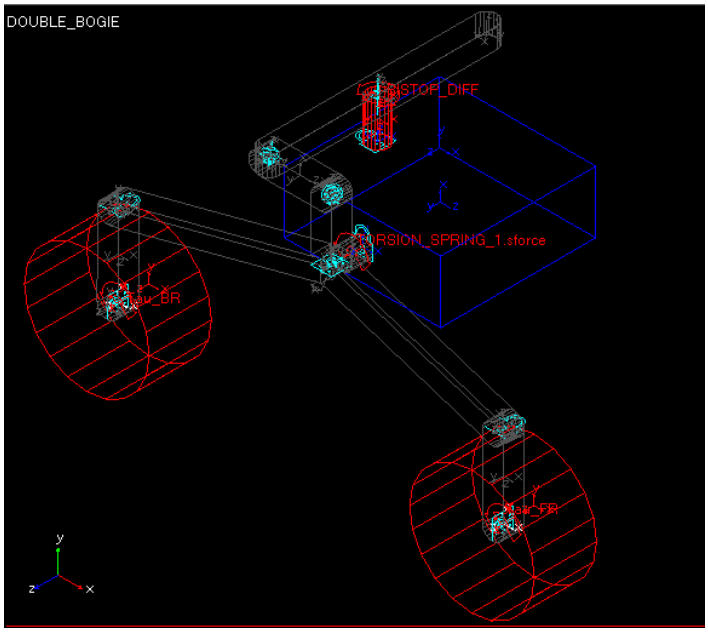


**Figure 6.6:** *2BG model topology*

Joint specifications are presented in the table below. The table referred to half-rover, in the complete model, each joint presents its symmetric counterpart.

**Table 6.2:** *2BG model topology specifications*

| **ID** | **Joint type** | **Body 1** | **Body 2** |
|---|---|---|---|
| J1 | Fixed | Core | Connector |
| J2 | Revolute | Connector | Bogie |
| J3 | Spherical | Bogie | Differential sys. link |
| J4 | Spherical | Differential sys. link | Differential bar |
| J5 | Revolute | Differential bar | Differential sys. hinge |
| J6 | Fixed | Differential sys. hinge | Core |
| J7 | Fixed | Bogie | Front wheel bracket |
| J8 | Revolute | Front wheel bracket | Front wheel |
| J9 | Fixed | Bogie | Back wheel bracket |
| J10 | Revolute | Back wheel bracket | Back wheel |

To enhance the physical realism of the simulation and prevent numerical divergence, the 2BG model adopts the same stabilization strategy used for the RB configuration. This transition from an ideal kinematic chain to a dynamic assembly is achieved by incorporating the following force-based elements:

- **Rotational Spring-Damper**: Joint **J2** is equipped with a torsional spring to replicate the inherent compliance of the bogie pivot. By utilizing the stiffness ($K_{spring}$) and damping ($C_{damp}$) coefficients established in the baseline model, the bogie maintains a stable yet flexible response when interacting with the terrain.

- **Mechanical Hard-Stops**: The range of motion of the differential system is regulated by a Two-sided impact function applied to the hinge (**J5**). This constraint enforces a $\pm 5°$ limit on the bar's rotation, preventing structural interference with the core. The impact logic remains grounded in the Hertzian contact parameters previously detailed, ensuring consistent behavior across different architectures.

### Actuation Setup

The actuation of the 2BG model is based on a four-wheel drive configuration where both propulsion and directional control are managed through the traction motors. Since this architecture lacks dedicated steering actuators, it utilizes a slip-steering logic, where the turning moment is generated by a velocity differential between the left and right wheel sets.

**Steering Logic** : To achieve the desired turning radius in the 2BG architecture, a slip-steering strategy is employed. Unlike the Rocker-Bogie, where the wheels are oriented toward the ICR, the 2BG wheels remain parallel to the rover's longitudinal axis. Consequently, the steering maneuver is generated by commanding a differential angular velocity between the internal and external wheel sets.

$$\omega_{target,i} = \frac{V_{des}}{R} \cdot \frac{R \pm w/2}{R_{wheel}} \tag{6.6}$$

In slip-steering architectures, the actual turning radius achieved by the rover is rarely identical to the theoretically commanded one. Due to the lateral friction and the lack of steerable wheels, the vehicle tends to follow a wider path than intended.

To compensate for this inefficiency and to bring the rover's performance closer to the original mission requirements, the target radius R is defined as:

$$R = \chi \cdot R_{baseline} \tag{6.7}$$

By setting $\chi = 0.30$ in the MATLAB script, the logic prescribes a turning radius that is 70% smaller than the original $R_{baseline}$. This over-steering command allows the rover to overcome the resistance of the fixed wheels and achieve an actual trajectory that more accurately matches the steering demands.

```
% Rover Parameter Definitions
L = 1850;           % [mm] Total length (front-to-rear axis)
W = 1250;           % [mm] Lateral track width
R_wheel = 300;      % [mm] Wheel radius

% Target Maneuver Parameters (from DRM)
V_cm_des = 1000;    % [mm/s] Desired rover CoM velocity
R_original = 11500; % [mm] Expected turning radius
chi = 0.31;         % [-] Scaling factor to overcome under/over
    steer
Radius = chi * R_original; % [mm] Target turning radius

% Calculations
% 1. Angular velocity of the rover about the ICR
% Omega = V / R
omega_rover = V_cm_des / Radius;

% 2. Target linear velocities for slip-steering
v_ext = omega_rover * (Radius + W/2); % Velocity for external side
v_int = omega_rover * (Radius - W/2); % Velocity for internal side

% 3. Target angular velocities (omega_target)
omega_target_ext = v_ext / R_wheel;   % [rad/s]
omega_target_int = v_int / R_wheel;   % [rad/s]
```

**Listing 6.2:** Slip-steering kinematic calculation

**Traction Torque** : The entire directional control is embedded within the traction torque commands. The four active motors (located at joints **J8** and **J10**) follow

the PD-based formulation previously defined in Equation 6.5.

### 6.2.3 Four wheel active model [4WA]

The 4-Wheel Active architecture is designed as a highly adaptable platform. Unlike the passive bogie-based systems, it utilizes four independent active legs to modify its geometric parameters in real-time, such as ground clearance and wheelbase, to suit specific mission requirements.

#### Specific Links and Inertial Properties

The model consists of a main chassis and four identical active suspension units. Each leg, shown in Figure 6.7, is composed of a fixed structural housing attached to the core and a pitching arm that connects directly to the wheel hub. Consistent with the other models, the links are modeled using Aluminum **6061-T6**, with a mass value for the link equal to $\mathbf{M_{4WAlink} = 2.3kg}$ .

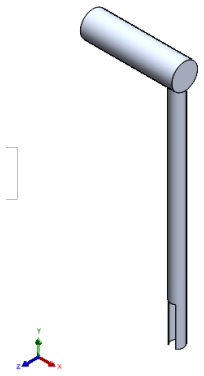

**Figure 6.7:** *4WA structure*

The inertia matrix of the component is:

$$\mathbf{I} = \begin{bmatrix} 1.66 \times 10^5 & I_{xy} & I_{xz} \\ -3.2 \times 10^4 & 2.9 \times 10^4 & I_{yz} \\ 0.01 & 0.27 & 1.8 \times 10^5 \end{bmatrix} \quad [\text{kg} \cdot \text{mm}^2]$$

### Assembly and Kinematic Topology

To facilitate active geometry reconfiguration, each corner of the main chassis is equipped with a pitching arm. This link is connected via a revolute joint that modulates the rover's stance, providing the necessary degrees of freedom for posture control without the added complexity of dedicated steering hardware.

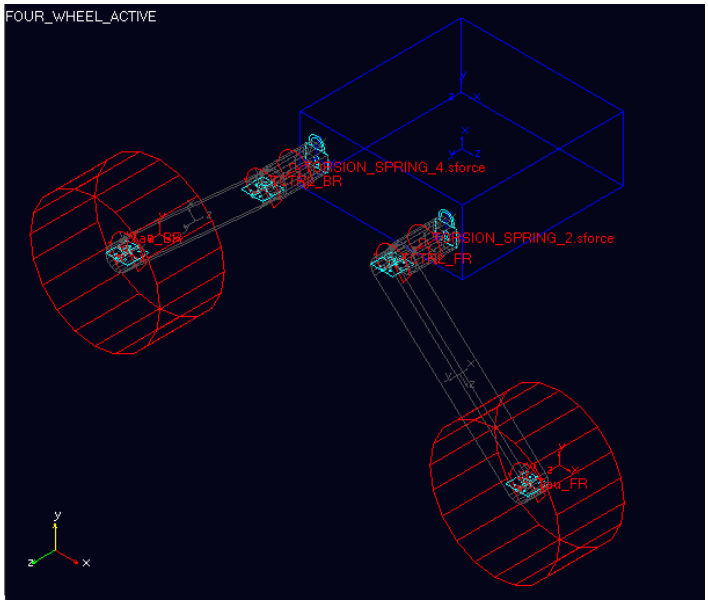


**Figure 6.8:** *4WA model topology*

The half-rover joints configuration shown in 6.8 is presented in Table 6.3:

**Table 6.3:** *4WA model topology specifications*

| ID | Joint type | Body 1 | Body 2 |
|---|---|---|---|
| J1 | Fixed | Core | Front connector |
| J2 | Revolute | Front Connector | Front Link |
| J3 | Revolute | Front Link | Front wheel |
| J4 | Fixed | Core | Back connector |
| J5 | Revolute | Back connector | Back link |
| J6 | Revolute | Back link | Back wheel |

To enhance the physical realism, 4WA model adopts one torsion spring for each active joint defined as follows:

**Rotational Spring-Damper**: Joints **J2** and **J3** are equipped with a torsional spring to account for compliance in controlled joints . It relies on the same stiffness ($K_{spring}$) and damping ($C_{damp}$) coefficients defined for previous model.

### Actuation Setup

The control architecture of the 4WA model is designed to leverage its active degrees of freedom to improve stability and terrain adaptability. The setup is divided into standard locomotion control and a specialized active pose control logic.

**Steering Logic** : The 4WA model adopts the same slip-steering logic previously defined for the 2BG architecture. Instead of utilizing dedicated steering actuators, directional control is achieved by commanding a velocity differential between the left and right wheel sets. The wheel setpoints follow the kinematic relations established in Equation 6.6 and the associated MATLAB implementation, ensuring that the rover achieves the desired trajectory while optimizing the overall mass budget by minimizing the number of motors.

**Traction Torque** : The propulsion is governed by the same torque control law established for the previous models (see Equation 6.5). This consistency ensures that any variation in performance during the maneuvers is strictly attributable to the different suspension topologies and their respective pose control strategies.

**Active Pose Control** : The defining feature of the 4WA model is the active management of its four pitching joints to maintain chassis stability and optimize wheel-soil interaction. The primary objective is pitch stabilization, ensuring the core remains as level as possible regardless of terrain slope. The control torques are modulated to meet the specific stabilization demands of each maneuver:

The control torques are modulated to meet the specific stabilization demands of each maneuver:

$$\tau_{ctrl} = -K_P^{ctrl} \cdot (\theta_{meas,i}^{pitch} - \theta_{target,i}) - K_D^{ctrl} \cdot \omega_{meas,i}^{pitch} \tag{6.8}$$

Where :

- $K_P^{ctrl}$ and $K_D^{ctrl}$ are the proportional and derivative gains, tuned to obtain the required adaptability of the system to external inputs (e.g., slopes,obstacles)

- $\theta_{target,i}$ is the target value to control the pitch of each leg. This value changes according to the action that DRM required and its defined as follow:

$$\theta_{target} = \pm\alpha + var_{corr}^{pitch} + var_{corr}^{h} \tag{6.9}$$

  Where $\alpha$ represents the rest angle, $var_{corr}^{pitch}$ and $var_{corr}^{h}$ are correction variables that influence respectively the pitch,by appling a gain to the road pitch measured angle, and the height position of the core, by adding or subtracting an angular offset to the rest position angle.

### 6.2.4 Hybrid model [HBD]

The Hybrid architecture represents the most advanced configuration in this study. It is designed as an articulated wheeled-legged hybrid, where each limb is not merely a structural support but a multi-jointed robotic chain. This configuration provides the highest degree of adaptability, allowing the system to decouple the control of ground clearance from the longitudinal footprint.

#### Specific Links and Inertial Properties

The HBD model consists of a central chassis and four identical articulated limbs. Each limb is subdivided into two main functional links to allow for complex reconfiguration. The two functional links are considered to be the same length, so each limbs presents two of the components shown in Figure 6.9. The material assigned to the part is **Al-6061 T6**, as done for other components, obtaining a mass value of $\mathbf{M_{HBDlink} = 2.9kg}$ .

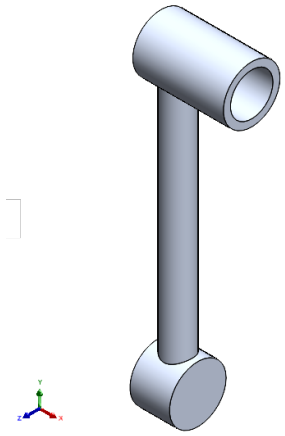

**Figure 6.9:** *HBD structure*

Inertia matrix obtained for the component is:

$$\mathbf{I} = \begin{bmatrix} 1.5 \times 10^5 & I_{xy} & I_{xz} \\ 1.1 \times 10^4 & 7.9 \times 10^3 & I_{yz} \\ 0.02 & 0.47 & 1.5 \times 10^5 \end{bmatrix} \quad [\text{kg} \cdot \text{mm}^2]$$

### Assembly and Kinematic Topology

The HBD topology features a redundant kinematic chain for each leg. Unlike the single-joint pitching of the 4WA, the HBD utilizes a coordinated triple-joint system per limb (6.10), allowing for independent control of the wheel's vertical position and longitudinal displacement.

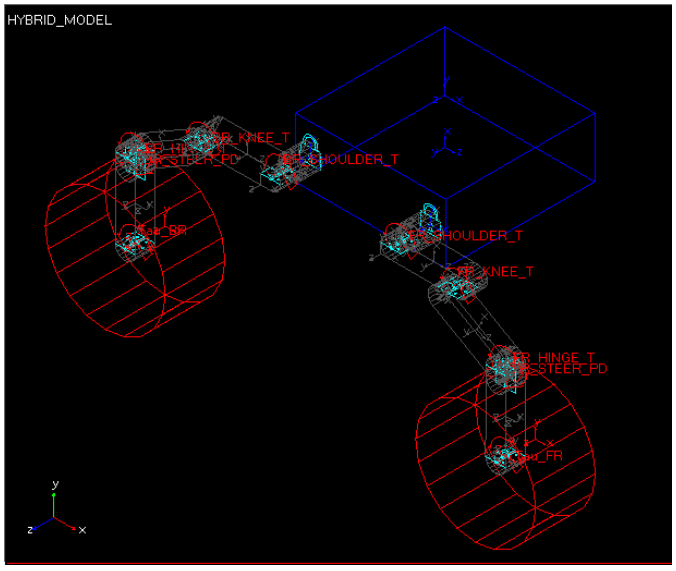


**Figure 6.10:** *HBD model topology*

Joints specifications for Hybrid model are reported in the Table 6.4 below:

**Table 6.4:** *HBD model topology specifications*

| ID | Joint type | Body 1 | Body 2 |
|---|---|---|---|
| J1 | Fixed | Core | Front connector |
| J2 | Revolute | Front Connector | Shoulder front link |
| J3 | Revolute | Shoulder front link | Knee front link |
| J4 | Revolute | Knee front link | Ankle front link |
| J5 | Revolute | Ankle front link | Front steer |
| J6 | Revolute | Front steer | Front wheel |
| J7 | Fixed | Core | Back connector |
| J8 | Revolute | Back Connector | Shoulder back link |
| J9 | Revolute | Shoulder back link | Knee back link |
| J10 | Revolute | Knee back link | Ankle back link |
| J11 | Revolute | Ankle back link | Back steer |
| J12 | Revolute | Back steer | Back wheel |

Unlike the previous architectures, the HBD model does not incorporate passive torsional springs or dampers. Given the high kinematic complexity and the large number of active degrees of freedom, the inclusion of passive elastic elements would interfere with the precise tuning of the control torques. Omitting these components ensures that the dynamic response is governed strictly by the active

control laws, avoiding potential inaccuracies in the torque computation and ensuring a transparent evaluation of the system's performance.

### Actuation Setup

**Steering Logic** : The HBD architecture adopts an explicit steering system like the one presented for the Rocker-Bogie model. To compute steering parameters, the system refers directly to the Double Ackermann kinematics presented for the Rocker-Bogie architecture. The integration of dedicated steering actuators allows each wheel to be physically oriented toward the ICR (Instantaneous Center of Rotation), ensuring pure rolling conditions and drastically reducing lateral scrubbing during directional maneuvers.

**Traction Torque** : The traction torque is regulated by the same formulation defined in Equation 6.5. Maintaining a unified traction logic is essential to isolate the impact of the articulated architecture on dynamic performance, ensuring that longitudinal velocity setpoints are comparable across all simulated platforms.

**Active Pose Control** : The defining feature of the HBD lies in the management of its 12 active posture joints. Thanks to the triple-joint configuration of each limb, the pose control is the primary variable defining the adaptive superiority of this model. The main objective is pitch stabilization, aimed at keeping the chassis stable and preventing excessive tilting during navigation over irregular terrain.

Control torques are defined as follow:

**Shoulder control equation**:

$$\tau_{ctrl}^{sh} = -K_{P_{sh}} \cdot (\theta_{meas.}^{sh} - \theta_{target}^{sh}) - K_{D_{sh}} \cdot \omega_{meas.}^{sh} \tag{6.10}$$

**Knee control equation**:

$$\tau_{ctrl}^{kn} = -K_{P_{kn}} \cdot (\theta_{meas.}^{kn} - \theta_{target}^{kn}) - K_{D_{kn}} \cdot \omega_{meas.}^{kn} \tag{6.11}$$

**Ankle control equation**:

$$\tau_{ctrl}^{an} = -K_{P_{an}} \cdot (\theta_{meas.}^{an} - \theta_{target}^{an}) - K_{D_{an}} \cdot \omega_{meas.}^{an} \tag{6.12}$$

The operational effectiveness of the model is determined by the logic governing the $\theta_{target}$ variables. Specifically, the setpoints for the upper joints are designed to share the reconfiguration load:

$$\theta_{target}^{sh} = \pm\alpha_1 \pm \frac{1}{2} var_{corr}^{pitch} \pm \frac{1}{2} var_{corr}^{h} \tag{6.13}$$

$$\theta_{target}^{kn} = \pm\alpha_2 \pm \frac{1}{2} var_{corr}^{pitch} \pm \frac{1}{2} var_{corr}^{h} \tag{6.14}$$

The ankle joint acts as a kinematic compensator to maintain the desired wheel orientation relative to the core:

$$\theta_{target}^{an} = \pm\theta_{meas}^{an-kn} \pm \theta_{meas}^{kn-sh} \tag{6.15}$$

Thanks to this control scheme, when a command for pitch or height variation is prescribed, the resulting motion is a coordinated composition of the movements of the shoulder and knee joints (e.g., joints **J2/J8** and **J3/J9**), balanced by the counter-rotation of the ankle joint (**J4/J10**). This geometric decoupling ensures that the rover can modify its stance without inducing parasitic rotations at the wheel-soil interface.

## 6.3 Numerical Setup and Physical Modeling

This section details the numerical strategies and physical parameters implemented within the MSC Adams environment to ensure simulation accuracy and solver stability.

### 6.3.1 Numerical Integration Strategy

The GSTIFF (Gear Stiff) integrator with the SI2 (Stabilized Index-2) formulation was selected for all simulation scenarios. This choice is specifically motivated by the presence of intermittent and non-linear contacts between the wheels and the terrain.

Unlike the standard I3 formulation, the SI2 formulation provides superior accuracy in calculating velocities and accelerations by controlling the error on the velocity states. This makes it significantly more robust for models where high-frequency oscillations, typical of solid-to-solid impacts and friction transitions, could otherwise lead to numerical instability or solver divergence.

### 6.3.2 Contact Mechanics and Friction Parameters

Since the primary focus of this study is the comparative analysis of rover architectures rather than the detailed design of the wheel geometry, the terrain has been modeled as a rigid surface. The interaction is governed by an impact function, as explained in chapter 3, with parameters tuned to approximate the mechanical behavior of a sandy terrain or lunar regolith simulant:

- Stiffness: $K = 500N/mm$
- Damping : $C_{max} = 5Ns/mm$
- Force exponent: $e = 1.2$
- Penetration depth: $d = 0.1mm$
- Static friction coefficient: $\mu_s = 0.9572$ [22]
- Dynamic friction coefficient: $\mu_d = 0.7972$[22]

These parameters were experimentally tuned to achieve an optimal balance between the physical realism of the wheel-soil interaction (approximating a compact terrain or lunar regolith) and the numerical stability of the solver. This calibration phase was fundamental to preventing numerical divergence and parasitic oscillations in the rover's response, ensuring high precision in the computation of control torques.

Due to the nature of solid-to-solid contact, the calculated forces exhibit inevitable high-frequency spikes when negotiating geometry transitions or obstacles (see Figure 6.11). These raw values have been appropriately filtered using a low-pass Butterworth filter to extract the meaningful steady-state loads required for motor sizing and stability assessment, as shown in Figure 6.12.

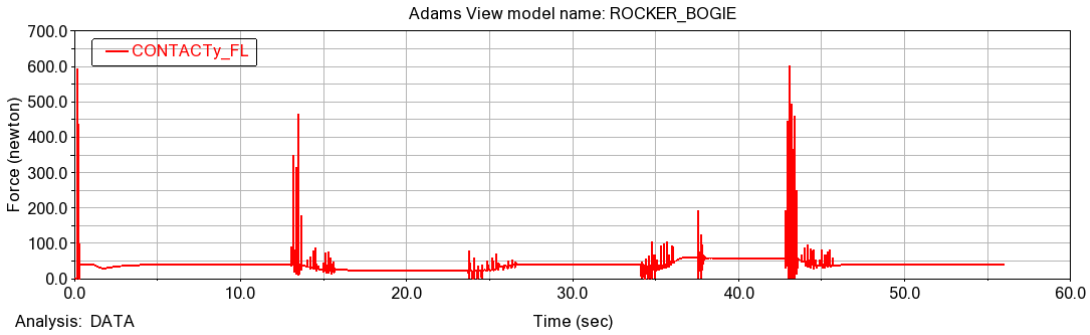


**Figure 6.11:** *Raw contact force example*

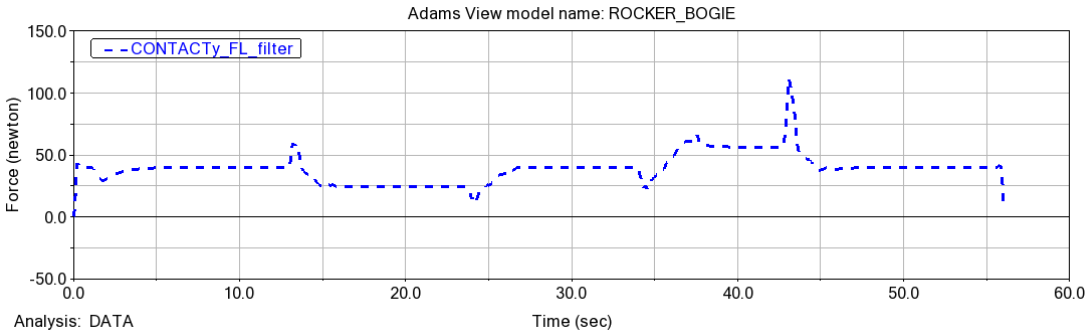


**Figure 6.12:** *Filtered contact force example*

### 6.3.3 Actuator Modeling

To maintain physical consistency, all propulsion, steering, and posture torques are implemented as Action-Reaction forces. Every control torque $\tau$ applied to a child link is balanced by an equal and opposite reaction torque $-\tau$ exerted on the parent link. This ensures that the internal loads are correctly accounted for within the kinematic chains, allowing the solver to accurately simulate the resulting disturbances on the rover's core during high-torque maneuvers or active reconfigurations.

# Chapter 7

# Results and Comparative Analysis

The study conducted aims to perform a comparative analysis among the four selected architectures for a rover developed for the lunar environment. In the following section, the performance of these rovers is evaluated with respect to the specific Design Reference Missions (DRMs).

## 7.1 Performance in DRM1

DRM1 was designed to validate the rover's capabilities to climb a slope simulating characteristic lunar crater values.

The metrics selected to evaluate the performance of each rover are explained in Chapter 5; here, the results for the four rovers, illustrated in Figure 7.1, are presented.

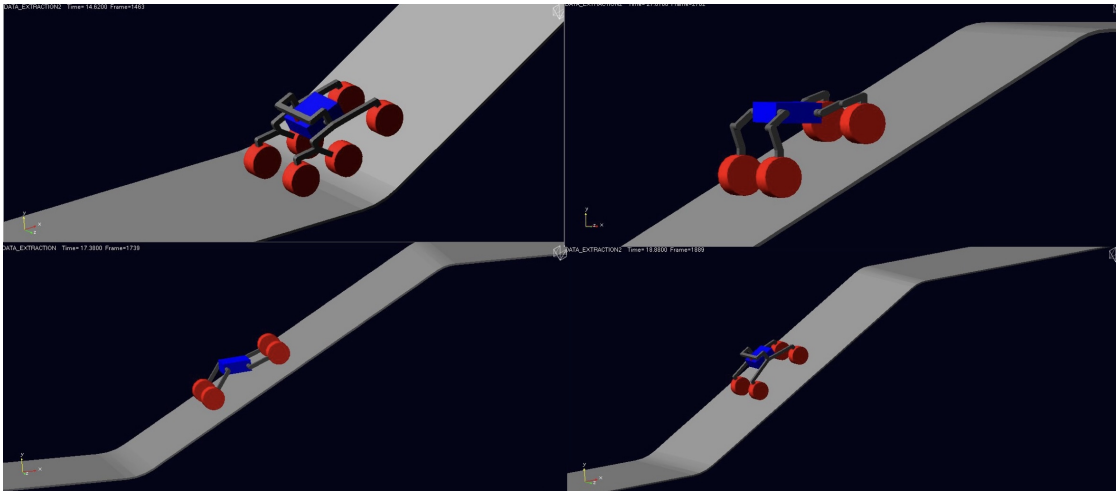

**Figure 7.1:** *Rovers model for DRM1*

The plots of the data extracted from the MSC Adams models were processed using MATLAB for presentation purposes. Specifically:

- **Critical velocity**: The critical velocity, $v_{crit}$, was determined experimentally by incrementally increasing the target speed of each rover while monitoring its dynamic behavior. The failure threshold was defined as the point at which the rover could no longer successfully complete the traverse (e.g., due to significant loss of traction or excessive deviation from the target path). The resulting critical velocity values are summarized in Table 7.1.

- **Acceleration RMS**: The RMS value of acceleration, assessing the stability of a payload on top of the rover:

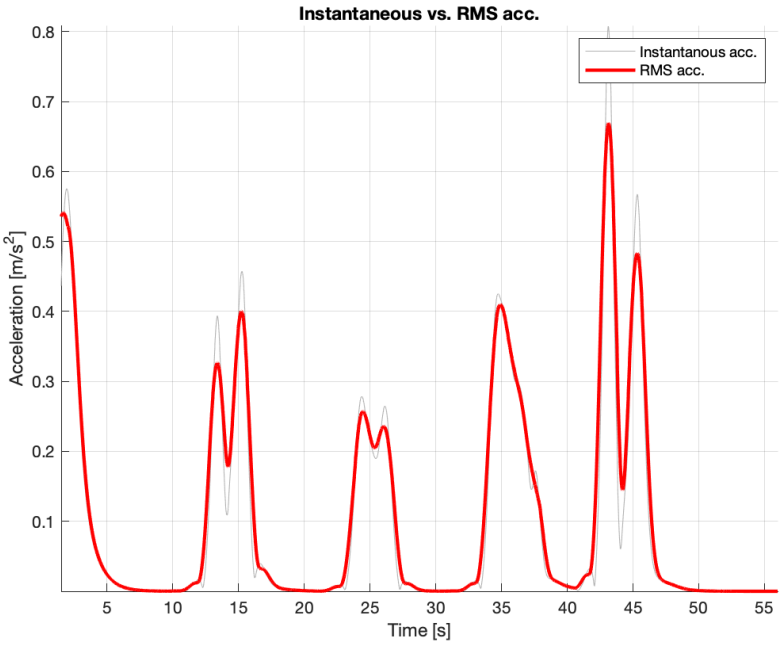


**Figure 7.2:** *RB acceleration RMS*

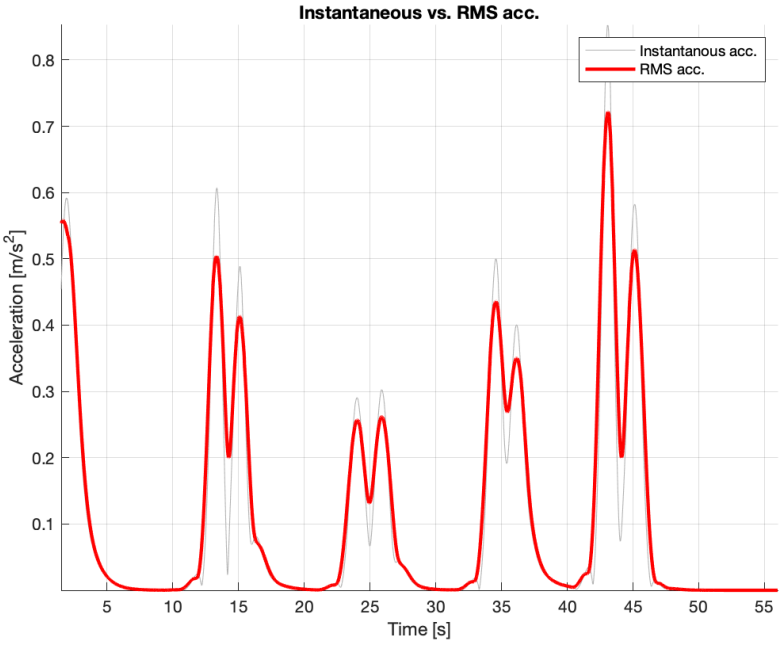


**Figure 7.3:** *2BG acceleration RMS*

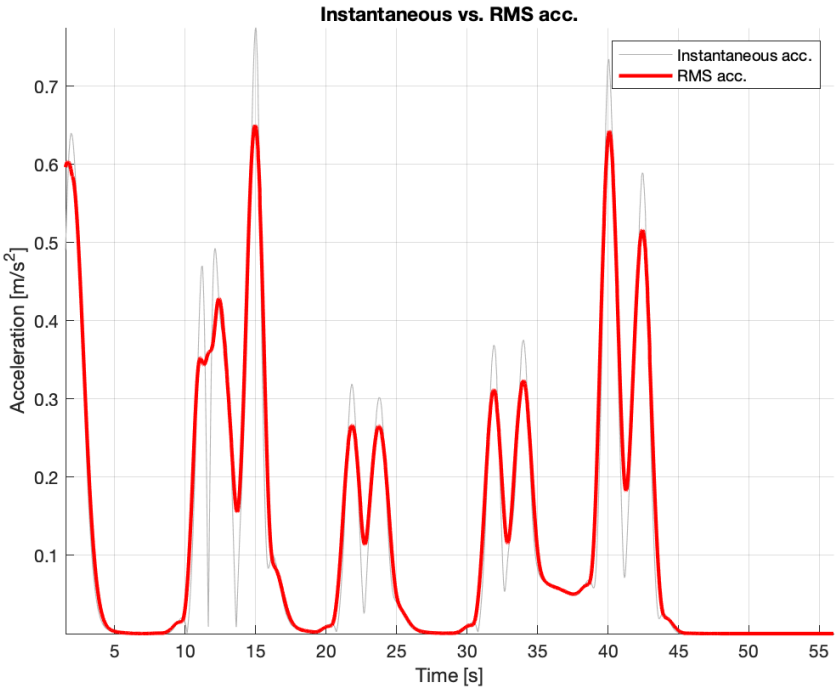


**Figure 7.4:** *4WA acceleration RMS*

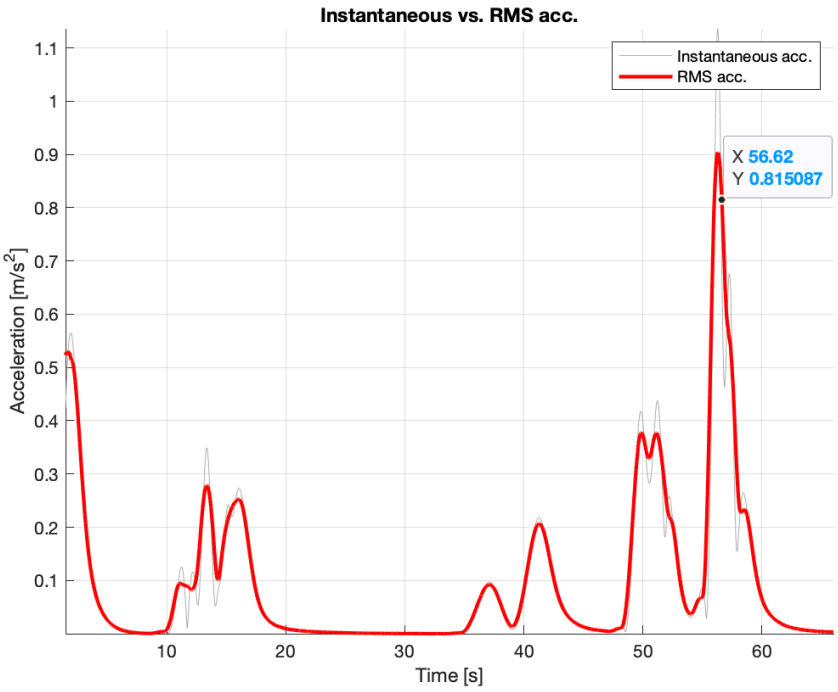


**Figure 7.5:** *HBD acceleration RMS*

- **Pitch Evolution**: The pitch evolution of each rover during the traverse of the slope, which is a specific metric for DRM1:

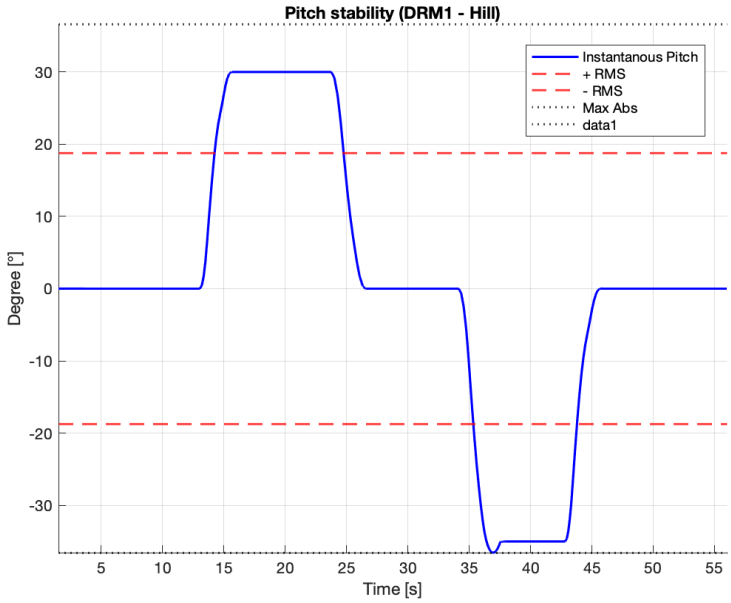


**Figure 7.6:** *RB pitch measure*

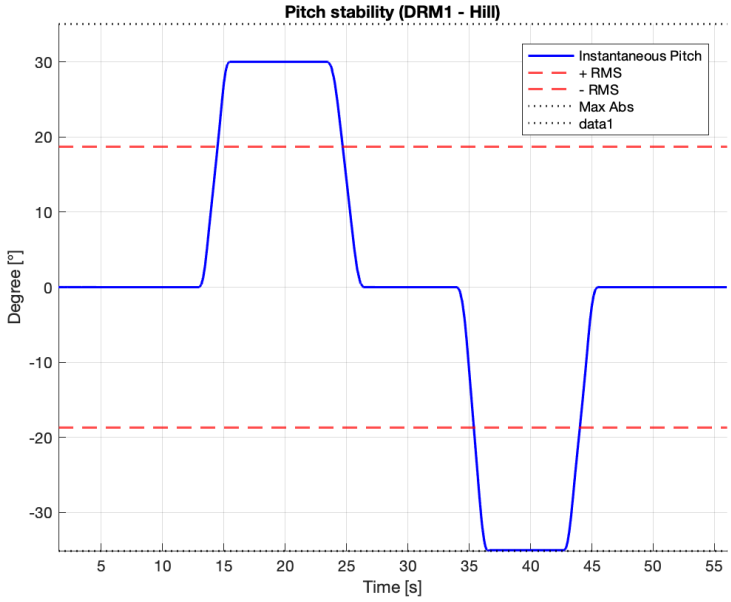


**Figure 7.7:** *2BG pitch measure*

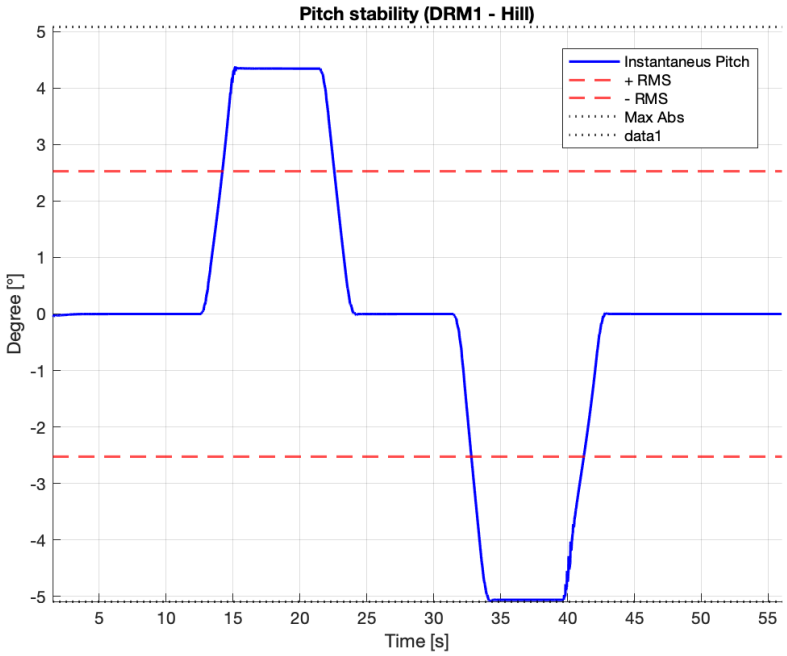


**Figure 7.8:** *4WA pitch measure*

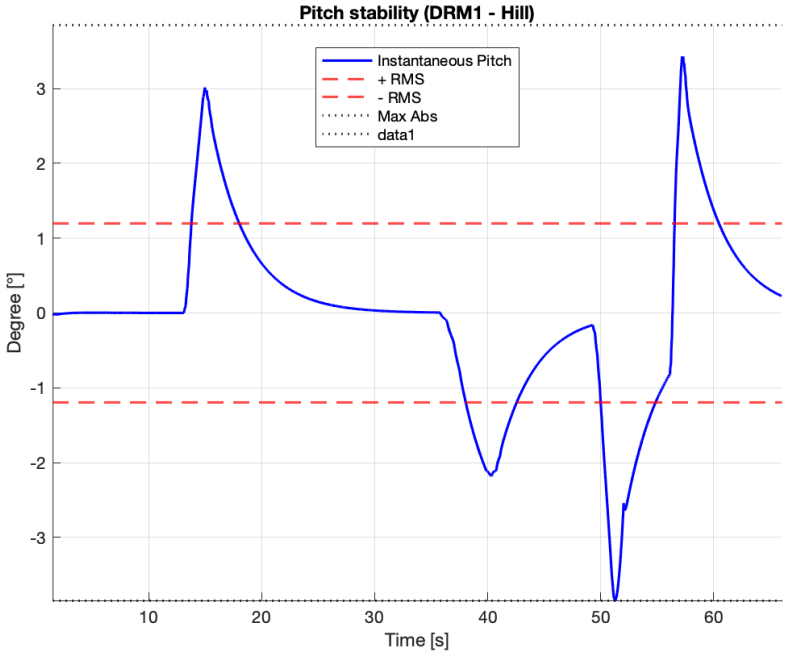


**Figure 7.9:** *HBD pitch measure*

- **Power Consumption**: The power measured over the entire simulation timespan, from which peak and mean values were extracted:

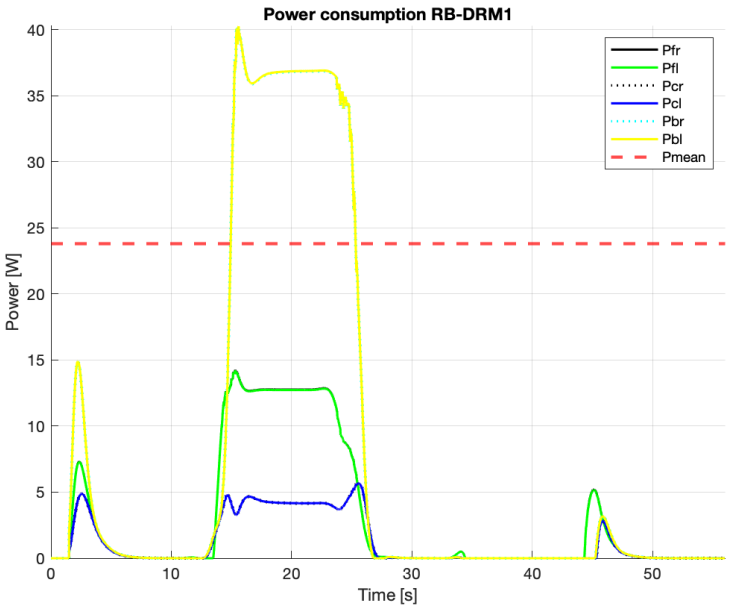


**Figure 7.10:** *RB power consumption*

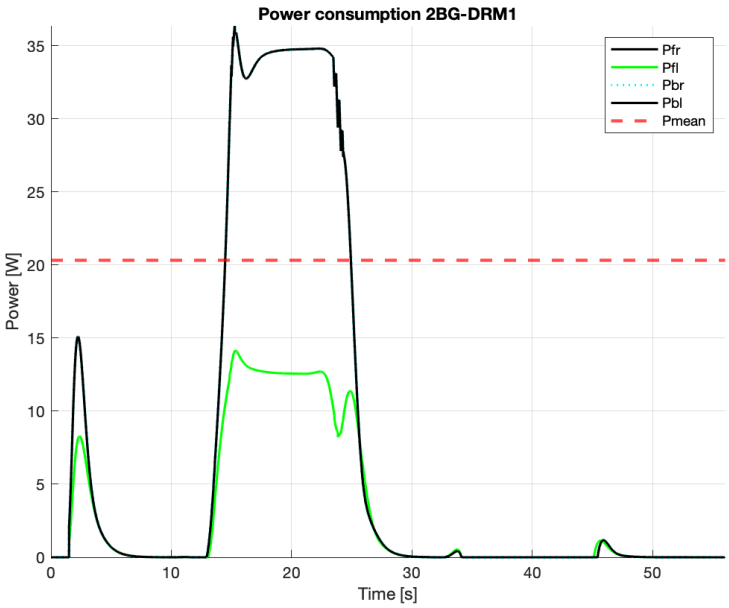


**Figure 7.11:** *2BG power consumption*


**Figure 7.12:** *4WA power consumption*

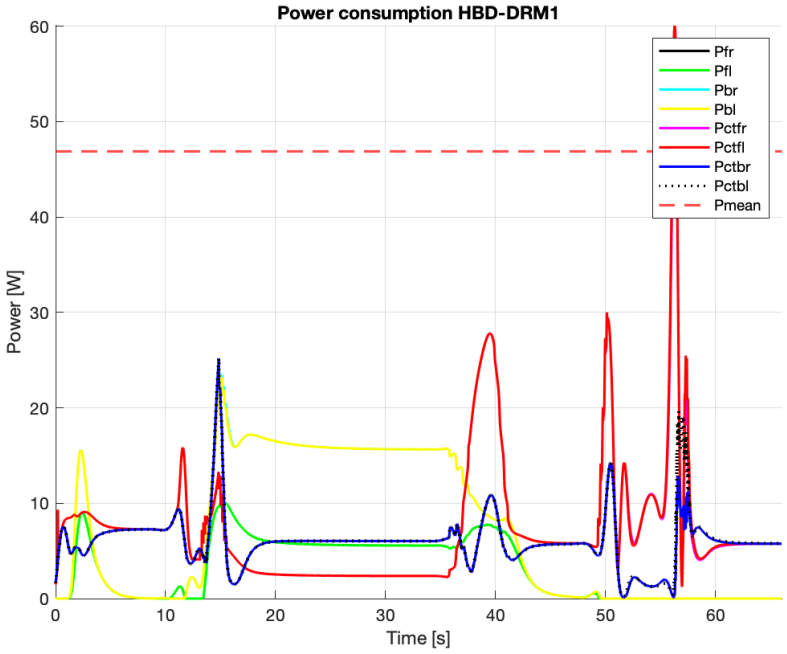


**Figure 7.13:** *HBD power consumption*

From these plots, the data for the comparative analysis were extracted and reported in Table 7.1 below, including the maximum speed evaluated in the MSC Adams environment, as explained in Section 5.2.2.

**Table 7.1:** *DRM1 raw data*

| COMPARISON MATRIX DRM1 | | | RAW | |
|---|---|---|---|---|
| Criteria | [RB] | [2BG] | [4WA] | [HBD] |
| SPEED [m/s] | 1,30 | 1,90 | 1,90 | 1,80 |
| STABILITY (aRMS) | 0,67 | 0,72 | 0,65 | 0,90 |
| PITCH RMS MAX [°] | 36,54 | 35,07 | 5,09 | 3,84 |
| PEAK POWER CONS [W] | 114,95 | 100,98 | 168,24 | 139,50 |
| MEAN POWER CONS. [W] | 23,80 | 20,34 | 55,56 | 46,88 |

To obtain comparable values from the aforementioned table, each element was normalized by row. Specifically, for metrics where superior performance is indicated by a higher value (higher-is-better), the reciprocal was used. This procedure ensured that all parameters were aligned within a common framework where a lower value consistently represents the optimal result. By establishing this uniform polarity, the data became directly comparable within the trade-off matrix, preventing any interpretational bias. The results were then summed by column to assess the performance of each architecture in this specific DRM and subsequently scaled from 0 to 10 for better readability.

**Table 7.2:** *DRM1 normalized data*

| COMPARISON MATRIX DRM1 | | | NORM. | |
|---|---|---|---|---|
| Criteria | [RB] | [2BG] | [4WA] | [HBD] |
| SPEED [m/s] | 0,19 | 0,28 | 0,28 | 0,26 |
| STABILITY (aRMS) | 0,27 | 0,25 | 0,28 | 0,20 |
| PITCH RMS MAX [°] | 0,05 | 0,06 | 0,38 | 0,51 |
| PEAK POWER CONS [W] | 0,27 | 0,31 | 0,19 | 0,23 |
| MEAN POWER CONS. [W] | 0,32 | 0,38 | 0,14 | 0,16 |
| Total | 1,11 | 1,27 | 1,26 | 1,36 |
| Sum/10 | 8,16 | 9,35 | 9,29 | 10,00 |

As shown in the table, all models exhibit high performance in the climbing

scenario, while the HBD architecture performs best due to the superior stability characteristics of its active system.

## 7.2 Performance in DRM2

In this reference mission, the rovers demonstrate the capability to negotiate various obstacles. Given the hazardous nature of such maneuvers, simulations were conducted at a controlled reference velocity of 0.1 m/s. As illustrated in Figure 7.14, the environment features obstacles of different heights symmetrically positioned along the rover's path to evaluate the response of the suspension system.

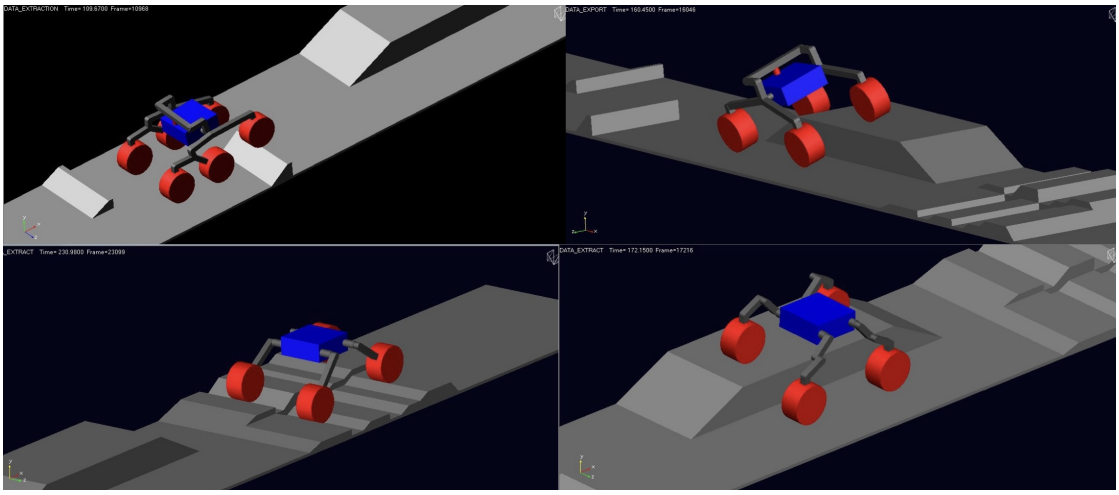

**Figure 7.14:** *Rovers model for DRM2*

Here the plots of the characteristic FoMs of this DRM are reported:

- **Critical velocity**:To verify the limit of the systems, critical velocity was evaluated also for DRM2, the values are reported in Table 7.3.

- **Acceleration RMS**: The RMS value of acceleration, computed as the section before, is presented here:

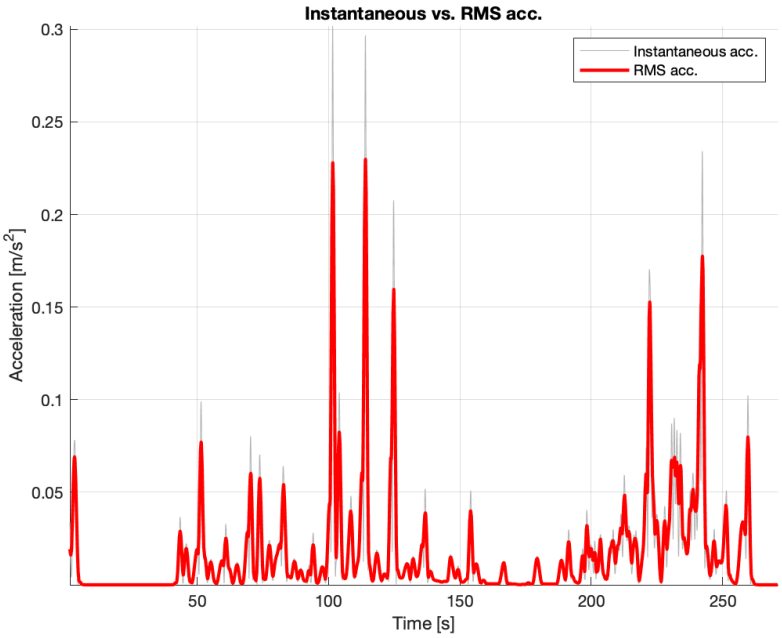


**Figure 7.15:** *RB acceleration RMS*

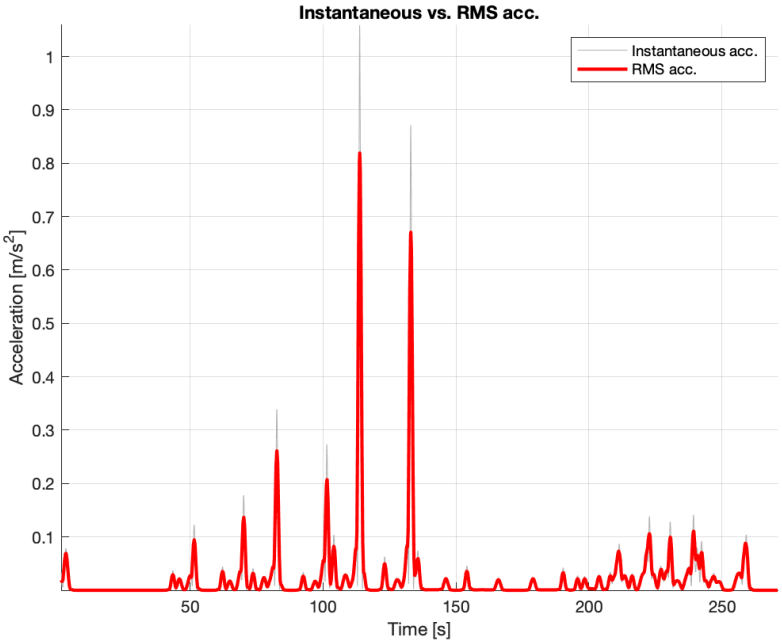


**Figure 7.16:** *2BG acceleration RMS*

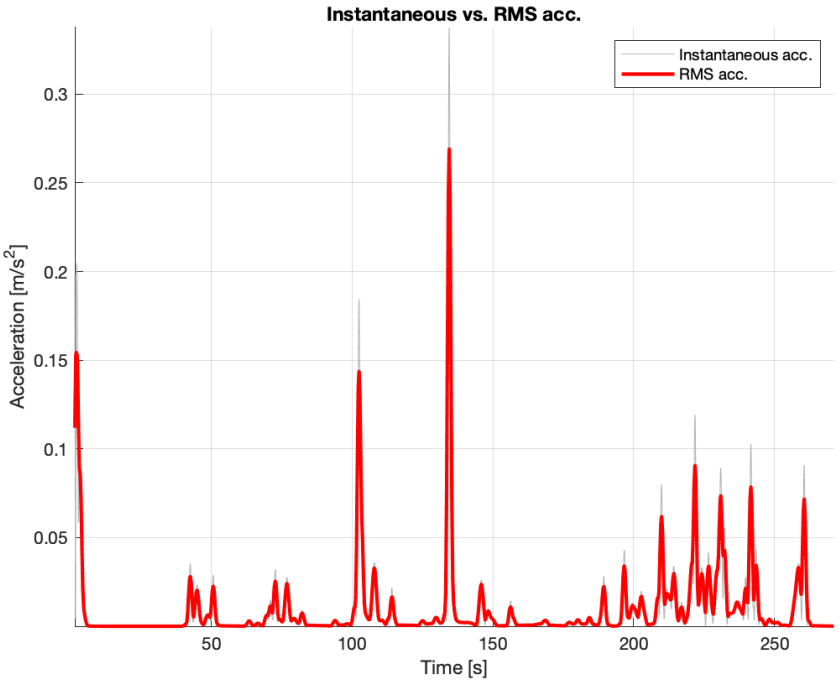


**Figure 7.17:** *4WA acceleration RMS*

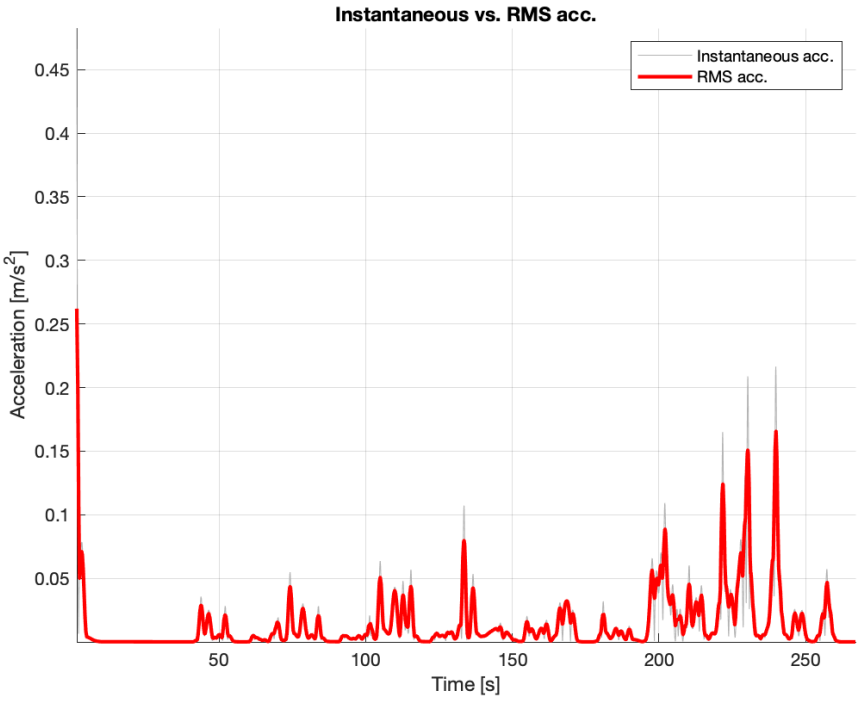


**Figure 7.18:** *HBD acceleration RMS*

- **Roll Evolution**: In this section, roll stability is evaluated instead of pitch stability evaluated for DRM1 as a more explanatory metric to understand rovers behaviour.

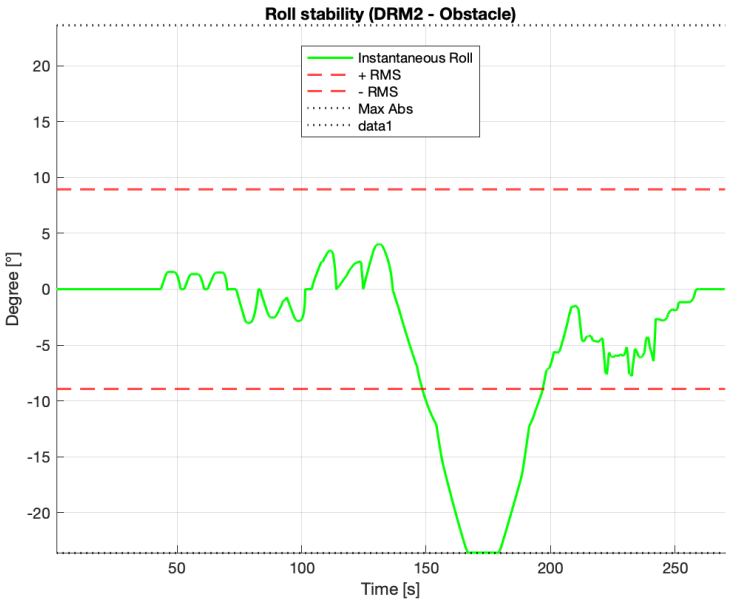


**Figure 7.19:** *RB roll measure*

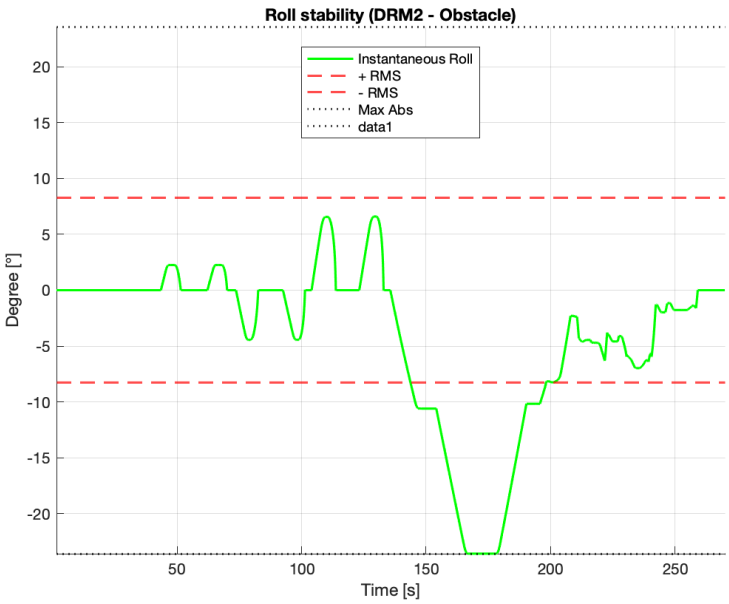


**Figure 7.20:** *2BG roll measure*


**Figure 7.21:** *4WA roll measure*


**Figure 7.22:** *HBD roll measure*

- **Power Consumption**: The power measured during the traverse of the trail are:

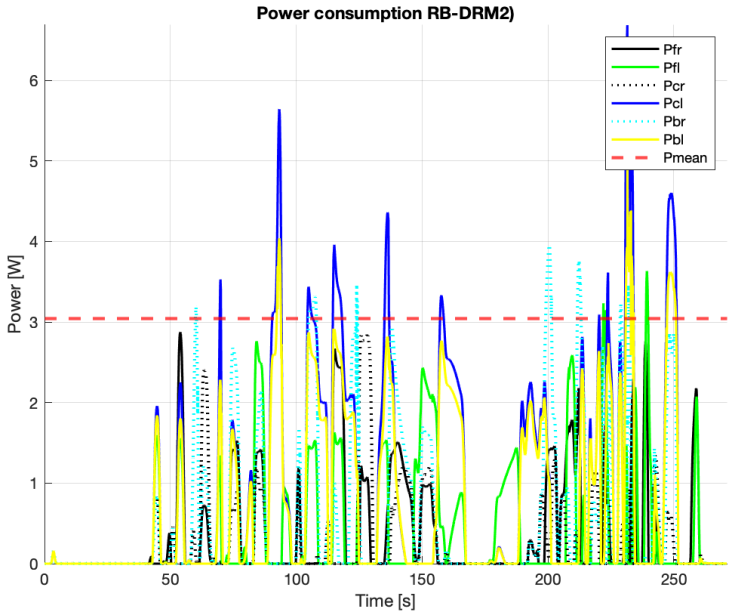


**Figure 7.23:** *RB power consumption*


**Figure 7.24:** *2BG power consumption*

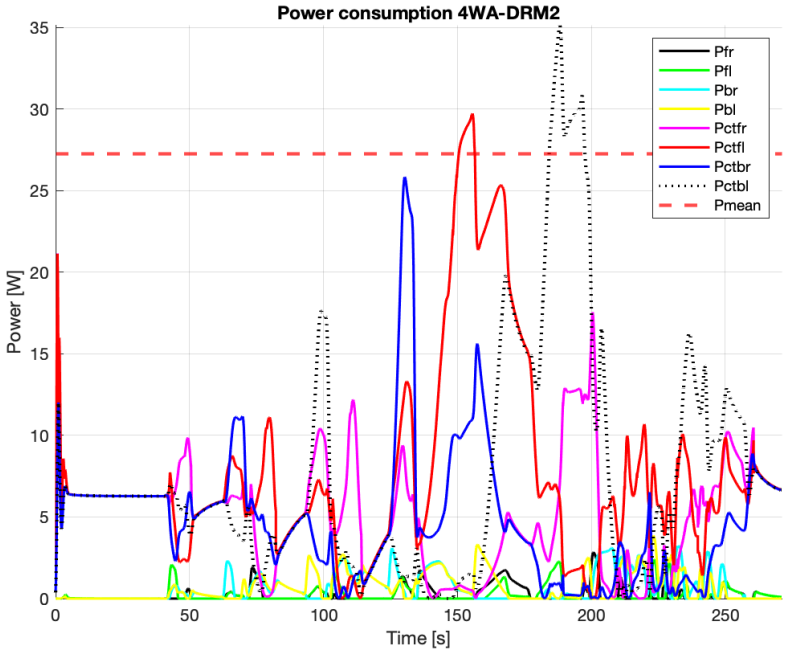


**Figure 7.25:** *4WA power consumption*

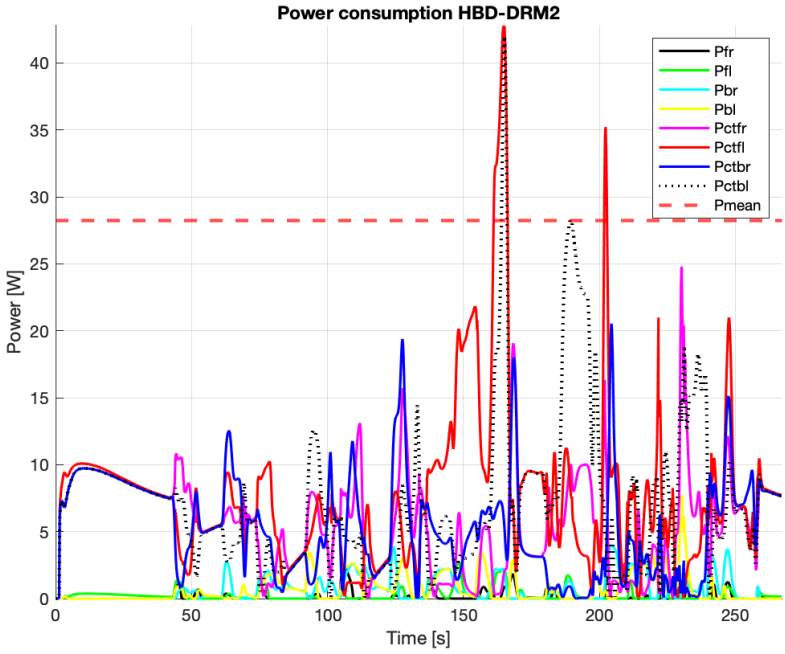


**Figure 7.26:** *HBD power consumption*

The summarizing table of raw data is reported below:

**Table 7.3:** *DRM2 raw data*

| COMPARISON MATRIX DRM2 | | | RAW | |
|---|---|---|---|---|
| Criteria | [RB] | [2BG] | [4WA] | [HBD] |
| SPEED [m/s] | 0,20 | 0,80 | 1,50 | 1,30 |
| STABILITY (aRMS) | 0,23 | 0,82 | 0,27 | 0,26 |
| ROLL RMS MAX [°] | 23,58 | 23,58 | 0,94 | 2,80 |
| MEAN POWER CONS. [W] | 3,05 | 1,57 | 27,26 | 28,26 |
| PEAK POWER CONS. [W] | 13,51 | 8,02 | 61,90 | 97,23 |

And therefore, the normalized value:

**Table 7.4:** *DRM2 normalized data*

| COMPARISON MATRIX DRM2 | | | NORM. | |
|---|---|---|---|---|
| Criteria | [RB] | [2BG] | [4WA] | [HBD] |
| SPEED [m/s] | 0,053 | 0,211 | 0,395 | 0,342 |
| STABILITY (aMS) | 0,332 | 0,093 | 0,284 | 0,291 |
| ROLL RMS MAX [°] | 0,028 | 0,028 | 0,706 | 0,238 |
| MEAN POWER CONS. [W] | 0,316 | 0,614 | 0,035 | 0,034 |
| PEAK POWER CONS. [W] | 0,329 | 0,554 | 0,072 | 0,046 |
| Total | 1,06 | 1,50 | 1,49 | 0,95 |
| Sum/10 | 7,05 | 10,00 | 9,94 | 6,34 |

As can be seen from Table 7.4, despite the performance of active rovers in maintaining a low values of roll angle, Double-Bogie performs better in general, thanks especially to the low level of power consumption metrics.

## 7.3 Performance in DRM3

All the data needed for comparison between models in DRM3 were extracted directly from MSC Adams by threshold setting and are reported in Table 7.6

- **Minimum steering radius**: evaluated by manually reducing the reference target radius, with a consequent change in the rover's steering angle and differential velocity

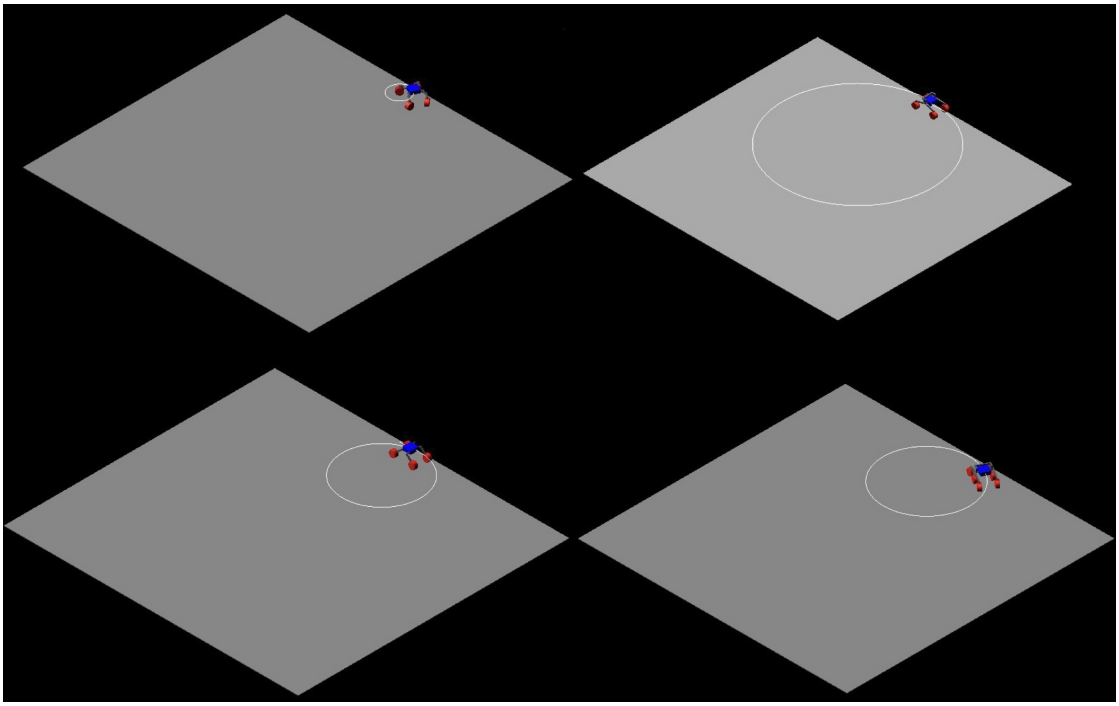

**Figure 7.27:** *Minimum steering radius evaluation*

- **Position error**: Obtained by measuring the results of the steering trajectory compared with the prescribed one.The black circle was placed in the model as a reference for the ideal path.

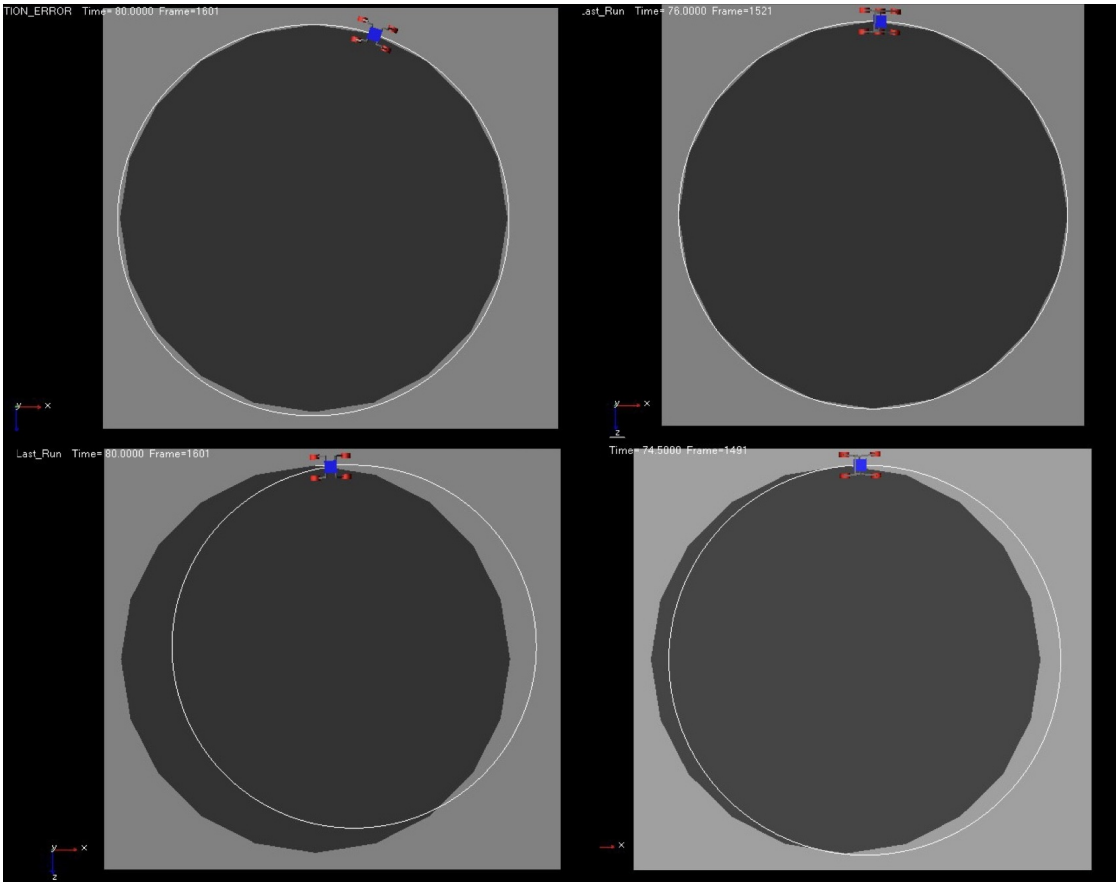

**Figure 7.28:** *Position error evaluation*

- **Slip stability**: The slip stability performances, evaluated with the same procedure used for critical velocity in DRM1 and DRM2, are then directly reported in Table 7.5.

**Table 7.5:** *DRM3 raw data*

| COMPARISON MATRIX DRM3 | | | RAW | |
|---|---|---|---|---|
| Criteria | [RB] | [2BG] | [4WA] | [HBD] |
| MIN. STEERING RADIUS [m] | 4,00 | 7,00 | 5,00 | 1,50 |
| POSITION ERROR [m] | 0,006 | 1,196 | 3,130 | 0,226 |
| SLIP STABILITY [m/s] | 2,00 | 1,00 | 1,30 | 1,50 |

And the normalized one:

**Table 7.6:** *DRM3 normalized data*

| COMPARISON MATRIX DRM3 | | | NORM. | |
|---|---|---|---|---|
| Criteria | [RB] | [2BG] | [4WA] | [HBD] |
| MIN. STEERING RADIUS [m] | 0,1985 | 0,1134 | 0,1588 | 0,5293 |
| POSITION ERROR [m] | 0,9702 | 0,0045 | 0,0017 | 0,0237 |
| SLIP STABILITY [m/s] | 0,3448 | 0,1724 | 0,2241 | 0,2586 |
| Total | 1,51 | 0,29 | 0,38 | 0,81 |
| Sum/10 | 10,00 | 1,92 | 2,54 | 5,36 |

Table 7.6 shows that systems equipped with explicit steering mechanism follows better the prescribed trajectory better, resulting in better general performance for Rocker-Bogie.

## 7.4 Static Performance Assessment

The last two metrics considered in this comparative analysis do not change according to the DRM but affect the comparison of the candidates architecture.

- **Mass**: Mass values are directly extracted from MSC Adams models and reported in Table 7.7

**Table 7.7:** *Architecture's mass comparison*

| **Architecture** | **Mass [kg]** |
|---|---|
| RB | 146 |
| 2BG | 128.6 |
| 4WA | 127.2 |
| HBD | 149.2 |

- **Complexity**: As already mentioned in 5 this FoM is based on pair-wise comparison matrix for the selected metrics. The scoring range varies from 2 to 4 or from 2 to 5, according to the metrics under consideration. The description of the scores is presented in Table 7.8

**Table 7.8:** *AHP scores for complexity evaluation*

| Sc. | P. of failure | Structure | N. actuators | Control |
|---|---|---|---|---|
| 1 | | | | |
| 2 | At least 3 less points of failure | Slightly lower structural complexity, comparable steering capabilities | Between 1 and 2 actuators less | Inverse Kinematics (IK) logic, high-frequency control |
| 3 | At least 5 less point o failure | Lower structural complexity, higher steering capabilities | Between 3 and 6 actuators less | Direct Kinematics (DK) logic and slippage control |
| 4 | At least 10 less point o failure | Linear load evolution, simpler structure | Between 7 and 9 actuators less | Traction and steering control only |
| 5 | | | Lower than 10 less actuators | |

According to the scoring system presented in Table 7.8, the pair-wise comparison matrices are presented below, the final values of each metric are computed by summing the column of pair-wise matrix, normalizing each column with respect to the sum of the raw column, then summing by rows and scaling to then for simplicity.

**Table 7.9:** *Pair-wise points of failure*

| Point of failure | RB | 2BG | 4WA | HBD |
|---|---|---|---|---|
| RB | 1,00 | 0,33 | 0,50 | 3,00 |
| 2BG | 3,00 | 1,00 | 0,50 | 4,00 |
| 4WA | 2,00 | 2,00 | 1,00 | 2,00 |
| HBD | 0,33 | 0,25 | 0,50 | 1,00 |
| sum col. | 6,33 | 3,58 | 2,50 | 10,00 |

| | | | | | sum row | norm/10 |
|---|---|---|---|---|---|---|
| N | 0,16 | 0,09 | 0,20 | 0,30 | 0,75 | 5,09 |
| O | 0,47 | 0,28 | 0,20 | 0,40 | 1,35 | 9,18 |
| R | 0,32 | 0,56 | 0,40 | 0,20 | 1,47 | 10,00 |
| M | 0,05 | 0,07 | 0,20 | 0,10 | 0,42 | 2,87 |

**Table 7.10:** *Pair-wise structure*

| Mech. struct. | RB | 2BG | 4WA | HBD |
|---|---|---|---|---|
| RB | 1,00 | 0,33 | 0,25 | 0,50 |
| 2BG | 3,00 | 1,00 | 0,50 | 3,00 |
| 4WA | 4,00 | 2,00 | 1,00 | 4,00 |
| HBD | 2,00 | 0,33 | 0,25 | 1,00 |
| sum col. | 10,00 | 3,67 | 2,00 | 8,50 |

| | | | | | sum row | norm/10 |
|---|---|---|---|---|---|---|
| N | 0,10 | 0,09 | 0,13 | 0,06 | 0,37 | 1,96 |
| O | 0,30 | 0,27 | 0,25 | 0,35 | 1,18 | 6,14 |
| R | 0,40 | 0,55 | 0,50 | 0,47 | 1,92 | 10,00 |
| M | 0,20 | 0,09 | 0,13 | 0,12 | 0,53 | 2,78 |

**Table 7.11:** *Pair-wise actuators*

| Actuators | RB | 2BG | 4WA | HBD |
|---|---|---|---|---|
| RB | 1,00 | 0,33 | 0,50 | 3,00 |
| 2BG | 3,00 | 1,00 | 3,00 | 5,00 |
| 4WA | 2,00 | 0,33 | 1,00 | 4,00 |
| HBD | 0,33 | 0,33 | 0,25 | 1,00 |
| sum col. | 6,33 | 2 | 4,75 | 13 |

| | | | | | sum row | norm/10 |
|---|---|---|---|---|---|---|
| N | 0,16 | 0,17 | 0,11 | 0,23 | 0,66 | 3,32 |
| O | 0,47 | 0,50 | 0,63 | 0,38 | 1,99 | 10,00 |
| R | 0,32 | 0,17 | 0,21 | 0,31 | 1,00 | 5,03 |
| M | 0,05 | 0,17 | 0,05 | 0,08 | 0,35 | 1,75 |

**Table 7.12:** *Pair-wise control*

| Control | RB | 2BG | 4WA | HBD |
|---|---|---|---|---|
| RB | 1,00 | 2,00 | 2,00 | 4,00 |
| 2BG | 0,50 | 1,00 | 3,00 | 3,00 |
| 4WA | 0,50 | 0,33 | 1,00 | 3,00 |
| HBD | 0,25 | 3,00 | 0,33 | 1,00 |
| sum col. | 2,25 | 6,33 | 6,33 | 11,00 |

| | | | | | sum row | norm/10 |
|---|---|---|---|---|---|---|
| N | 0,44 | 0,32 | 0,32 | 0,36 | 1,44 | 10,00 |
| O | 0,22 | 0,16 | 0,47 | 0,27 | 1,13 | 7,82 |
| R | 0,22 | 0,05 | 0,16 | 0,27 | 0,71 | 4,90 |
| M | 0,11 | 0,47 | 0,05 | 0,09 | 0,73 | 5,06 |

The total complexity metric is then computed to be a parameter of the global comparative analysis, obtaining the following results:

**Table 7.13:** *Total complexity matrix*

| | RB | 2BG | 4WA | HBD |
|---|---|---|---|---|
| failure | 0,7509 | 1,3528 | 1,4739 | 0,4224 |
| struct | 0,3747 | 1,1757 | 1,9160 | 0,5336 |
| actuators | 0,6606 | 1,9899 | 1,0007 | 0,3489 |
| control | 1,4397 | 1,1265 | 0,7055 | 0,7283 |
| | 3,2259 | 5,6448 | 5,0961 | 2,0331 |

As expected, double bogie architecture is the simplest one, due to the fewer joints and actuators and the skid steering capability.

# Chapter 8

# Conclusions and Future Work

## 8.1 Conclusions

This concluding section provides a comparative synthesis of the different mobility architectures analyzed throughout this study. The objective is to integrate the dynamic performance results obtained across the Design Reference Missions (DRMs) with static architectural metrics to establish a holistic performance framework. By performing a comprehensive trade-off analysis, this chapter identifies the configuration that offers the optimal balance between operational efficiency and design feasibility, addressing the core requirements of the mission.

Here, Table 8.1 links the architectures with global performances:

**Table 8.1:** *Architecture's comparison matrix*

| COMPARISON MATRIX ARCHITECTURE | | | RAW | |
|---|---|---|---|---|
| Criteria | [RB] | [2BG] | [4WA] | [HBD] |
| DRM1 | 1,108 | 1,271 | 1,262 | 1,358 |
| DRM2 | 1,058 | 1,500 | 1,491 | 0,951 |
| DRM3 | 1,513 | 0,290 | 0,385 | 0,812 |
| MASS | 0,007 | 0,008 | 0,008 | 0,007 |
| COMPLEXITY | 3,226 | 5,645 | 5,096 | 2,033 |

And then, for clarity of interpretation, the normalized one.

**Table 8.2:** *Normalized architecture's comparison matrix*

| COMPARISON MATRIX ARCHITECTURE | | | NORM. | |
|---|---|---|---|---|
| Criteria | [RB] | [2BG] | [4WA] | [HBD] |
| **DRM1** | 0,22 | 0,25 | 0,25 | 0,27 |
| **DRM2** | 0,21 | 0,30 | 0,30 | 0,19 |
| **DRM3** | 0,50 | 0,10 | 0,13 | 0,27 |
| **MASS** | 0,23 | 0,27 | 0,27 | 0,23 |
| **COMPLEXITY** | 0,20 | 0,35 | 0,32 | 0,13 |
| Total | 1,37 | 1,27 | 1,27 | 1,09 |
| **Sum/10** | **10,00** | **9,24** | **9,22** | **7,93** |

In conclusion, the comparative analysis identifies the Rocker-Bogie architecture as the optimal configuration for the mission objectives, as can be seen from Table 8.2. While other models exhibited peak performance in specific DRM scenarios, the Rocker-Bogie provides the best overall balance between obstacle negotiation, slope climbing, and steering capabilities. It is important to note that this comparative analysis is intended to present unbiased data, as no specific weighting was applied to the performance metrics. Consequently, the final ranking could change significantly if a specific mission were to prioritize certain criteria over others, for instance, favoring high-slope stability over power consumption or structural simplicity. This study therefore provides a neutral baseline for future decision-making based on specific mission requirements. In accordance with Systems Engineering methodologies, it is crucial to recognize that the 'best' rover is not necessarily the one achieving the highest results across all performance fronts. Instead, the optimal architecture is defined by its ability to balance competing requirements effectively, ensuring a robust and reliable solution that meets the global mission objectives rather than merely optimizing individual metrics.

## 8.2 Future Work

To further enhance the fidelity of the simulation and bridge the gap between virtual prototyping and physical testing, the research can be extended through

- **Advanced Soil Interaction Model**:
  - ATV-Module integration: Future models could replace the rigid terrain assumption by integrating the Adams Tracked Vehicle (ATV) module. This would allow for the implementation of "soft soil" models (such as Bekker-Wong) to simulate sinkage and rolling resistance in lunar regolith.
  - DEM Co-simulation: Performing co-simulations implementing the Discrete Element Method (DEM) to evaluate wheel-soil interaction at a particle level. This approach requires a more detailed wheel model, including grousers and specific tread geometries.
- **Model Improvements**: The current torque-based actuators can be refined through Adams-MATLAB co-simulation. This setup would enable the implementation of realistic traction control systems to manage slip and optimize torque distribution.
- **Hybrid Locomotion Mode**: For the HBD architecture, a walking gait could be developed using Inverse Kinematics (IK). By locking wheel rotation and moving the legs as a quadruped, the rover could navigate extreme terrains inaccessible for traditional rolling systems.
- **Optimization of Control Architectures**:Moving from independent PID loops to more integrated architectures, such as Model Predictive Control (MPC), via co-simulation. These strategies can significantly improve stability and energy efficiency during complex maneuvers.

# Bibliography


[1] NASA. *Artemis: Returning Humans to the Moon*. Accessed: March. 1, 2026. 2024. URL: https://www.nasa.gov/humans-in-space/artemis/ (cit. on p. 1).

[2] European Space Agency. *Moonlight*. Accessed: March. 1, 2026. 2024. URL: https://www.esa.int/Applications/Connectivity_and_Secure_Communications/Moonlight (cit. on p. 1).

[3] M. Elvis, T. Milligan, and A. Krolikowski. «The peaks of eternal light: A near-term property issue on the moon». In: *Space Policy,Volume 38, Pages 30-38,ISSN 0265-9646, https://doi.org/10.1016/j.spacepol.2016.05.011.* (2016) (cit. on p. 1).

[4] H.M. Brown, A.K. Boyd, B.W. Denevi, M.R. Henriksen, M.R. Manheim, M.S. Robinson, E.J. Speyerer, and R.V. Wagner. «Resource Potential of Lunar Permanently Shadowed Regions.» In: *Icarus (New York, N.Y. 1962), vol. 377, no. 114874, https://doi.org/10.1016/j.icarus.2021.114874.* (2022) (cit. on p. 1).

[5] *Adams 2023.3/Adams View User's Guide*. MSC Adams documentation. MSC Software. 2023 (cit. on p. 3).

[6] Simon Kassel. *Lunokhod-1 Soviet Lunar Surface Vehicle*. Sept. 1971 (cit. on p. 5).

[7] L. Chunlai et al. «The Chang'e 3 Mission Overview». In: *Space science reviews, 2015-07, Vol.190 (1-4), p.85-101, https://doi.org/10.1007/s11214-014-0134-7.* (2015) (cit. on p. 5).

[8] Q. Wang and J. Liu. «A Chang'e-4 mission concept and vision of future Chinese lunar exploration activities». In: *Acta Astronautica,Volume 127,Pages 678-683,ISSN 0094-5765,https://doi.org/10.1016/j.actaastro.2016.06.024.* (2016) (cit. on p. 5).

[9] Indian Space Research Organisation. *Chandrayaan-3 Details*. 2023. URL: https://www.isro.gov.in/Chandrayaan3_Details.html (cit. on p. 6).

[10] Anthony Colaprete. *Volatiles Investigating Polar Exploration Rover (VIPER)*. Apr. 2021 (cit. on p. 6).

[11] NASA Jet Propulsion Laboratory. *Mars Pathfinder / Sojourner Rover*. 1997. URL: https://www.jpl.nasa.gov/missions/mars-pathfinder-sojourner-rover/ (cit. on p. 6).

[12] NASA. *Mars Exploration Rovers: Spirit and Opportunity*. 2003. URL: https://science.nasa.gov/mission/mars-exploration-rovers-spirit-and-opportunity/ (cit. on p. 6).

[13] NASA. *Mars Science Laboratory (MSL) Curiosity*. 2011. URL: https://science.nasa.gov/mission/msl-curiosity/ (cit. on p. 6).

[14] NASA. *Mars 2020 Perseverance Rover*. 2020. URL: https://science.nasa.gov/mission/mars-2020-perseverance/ (cit. on p. 6).

[15] Basilio Bona. *Dynamic Modelling of Mechatronic Systems*. Torino, Italy: CELID, 2018 (cit. on p. 11).

[16] *Adams 2022.4/Adams Solver User's Guide*. MSC Adams documentation. MSC Software. 2022 (cit. on p. 13).

[17] Richard G. Budynas and J. Keith Nisbett. *Shigley's Mechanical Engineering Design*. Ninth. New York, NY: McGraw-Hill Education, 2011 (cit. on p. 15).

[18] Norman S. Nise. *Control Systems Engineering*. 7th. Hoboken, NJ: Wiley, 2015 (cit. on p. 22).

[19] *Expanded Guidance for NASA Systems Engineering: Volume 1 – Systems Engineering Practices*. Tech. rep. NASA, 2016 (cit. on p. 25).

[20] T. L. Saaty. «Decision making — the Analytic Hierarchy and Network Processes (AHP/ANP)». In: *Journal of Systems Science and Systems Engineering* 13 (2004) (cit. on p. 27).

[21] Siciliano Bruno. *Robotics: Modelling, Planning and Control*. Springer, 2010 (cit. on p. 52).

[22] J. Bendixen Noe, P. van Susante, Sibille, and L.Pinto-Reveggino J. «Static and kinetic friction coefficients for regolith delivery into a molten regolith electrolysis reactor». In: *Earth and Space 2022 (pp. 106-119)* (2022) (cit. on p. 67).